First print - corrections
Corrections are marked.

Physics of Photonic Devices

SHUN LIEN CHUANG
Professor of Electrical and Computer Engineering
University of Illinois at Urbana-Champaign

WILEY
A JOHN WILEY & SONS, INC., PUBLICATION

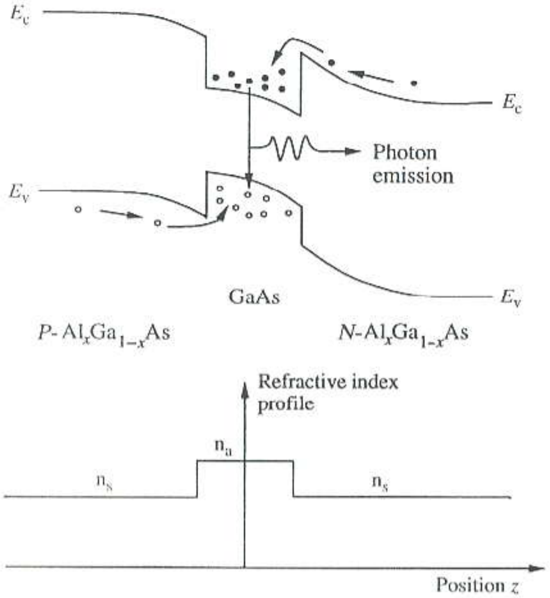

Figure 1.7 A double-heterojunction semiconductor laser structure, where the central GaAs region provides both the carrier confinement and optical confinement because of the conduction and valence band profiles and the refractive index profile. This double confinement enhances stimulated emissions and the optical modal gain.

The control of the mole fractions of different atoms also makes the band-gap engineering extremely exciting. For optical communication systems, it has been found that minimum attenuation [19] in the silica optical fibers occurs at 1.30 μm and 1.55 μm (Fig. 1.8a). The dispersion of light at 1.30 μm is actually zero (Fig. 1.8b). It is therefore natural to design sources such as light-emitting diodes and laser diodes, semiconductor modulators, and photodetectors operating at these desired wavelengths. In addition, many wavelengths, or the so-called optical channels for dense wavelength-division multiplexing (DWDM) applications, near 1550 nm with constant frequency spacing such as 50, 100, or 200 GHz can be used to take advantage of the broad 24 THz frequency bandwidth near the minimum attenuation. For example, by controlling the mole fraction of gallium and indium in an $In_{1-x}Ga_xAs$ material, a wide tunable range of band gap is possible because InAs has a 0.354 eV band gap and GaAs has a 1.424 eV band gap at room temperature. The lattice constant of the ternary alloy has a linear dependence on the mole fraction

$$a(A_xB_{1-x}C) = x\,a(A\overset{C}{\cancel{B}}) + (1-x)\,a(BC) \qquad (1.3.1)$$

C where $a(A\cancel{B})$ is the lattice constant of the binary compound $A\cancel{B}$ and $a(BC)$ is that of the C compound BC. This linear interpolation formula works very well for the lattice constant, but not for the band gap. For the band-gap dependence, a quadratic dependence

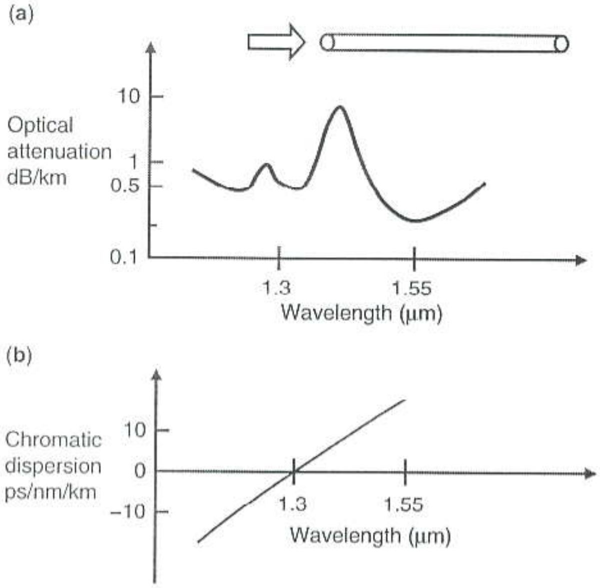

Figure 1.8 Simplified illustrations of (a) attenuation spectrum and (b) the dispersion parameter of light propagating in silica optical fiber.

on the mole fraction x is usually required (see Appendices C and D on pages 801–809 for some important material systems)

C

$$E_g(A_xB_{1-x}C) = x\,E_g(A\cancel{B}) + (1-x)\,E_g(BC) - bx(1-x) \qquad (1.3.2)$$

where b is called the bowing parameter because it causes a deviation of the ternary band-gap energy away from a linear interpolation of the two band-gap energies of the binary compounds. Figure 1.9 plots the band-gap energy at $T = 0\text{K}$ as a function of the lattice constant for many binary and ternary compound semiconductors [20]. For example, GaAs has a band gap of 1.519 eV at low temperature and a lattice constant of 5.6533 Å, whereas InAs has a band gap of 0.417 eV and a lattice constant of 6.0584 Å, as indicated. A ternary $\text{In}_{1-x}\text{Ga}_x\text{As}$ compound has the two end points at GaAs ($x = 0$) and InAs ($x = 1$) and its band gap has a slight downward bowing below a linear interpolation. At $x = 0.468$, the $\text{In}_{0.532}\text{Ga}_{0.468}\text{As}$ alloy has a lattice constant matched to that of the InP (5.8688 Å).

For $\text{Al}_x\text{Ga}_{1-x}\text{As}$ ternary compounds with $0 \leq x < 0.4$, the following formula is commonly used at room temperature:

$$E_g(\text{Al}_x\text{Ga}_{1-x}\text{As}) = 1.424 + 1.247x \ \text{(eV)}. \qquad (1.3.3)$$

Most ternary compounds require a quadratic term because the bowing parameter is not zero. From the above formula, we can calculate the conduction and valence band edge discontinuities between a GaAs and an $\text{Al}_x\text{Ga}_{1-x}\text{As}$ heterojunction using

1. **Electron Capture:** An electron in the conduction band recombines with a hole in the valence band and releases its energy to a nearby electron. This process destroys an electron–hole pair. The recombination rate is

$$R_n = C_n n^2 p. \tag{2.3.13}$$

   An important Auger process, called CHCC process, is shown in Fig. 2.7a in the momentum space. An electron (1) in the conduction (C) band interacts with another electron (2) in the conduction (C) band via Coulomb interaction, resulting in the recombination of electron (2) with a heavy (H) hole in the valence band (2′). The emitted band-gap energy due to this electron–hole recombination is picked up by electron (1) being excited to a higher energy state (1′). In this process, the hole density in the heavy-hole band and the electron density in the conductor band should be used in (2.3.13).

2. **Electron Emission:** An incident (energetic) electron in the conduction band creates impact ionization by breaking a bond, thus causing an electron in the valence band jump to the conduction band. This process creates an electron–hole pair. The generation rate is

$$G_n = e_n n. \tag{2.3.14}$$

3. **Hole Capture:** An electron in the conduction band recombines with a hole in the valence band with the released energy taken up by a nearby hole. This process destroys an electron–hole pair. The recombination rate is

$$R_p = C_p n p^2. \tag{2.3.15}$$

   Two important Auger processes related to hole captures, called CHSH and CHLH processes, are shown in Fig. 2.7b and Fig. 2.7c, respectively. In the CHSH process, a conduction (C) band electron recombines with a heavy hole (H), and the emitted band-gap energy is picked up by a nearby heavy

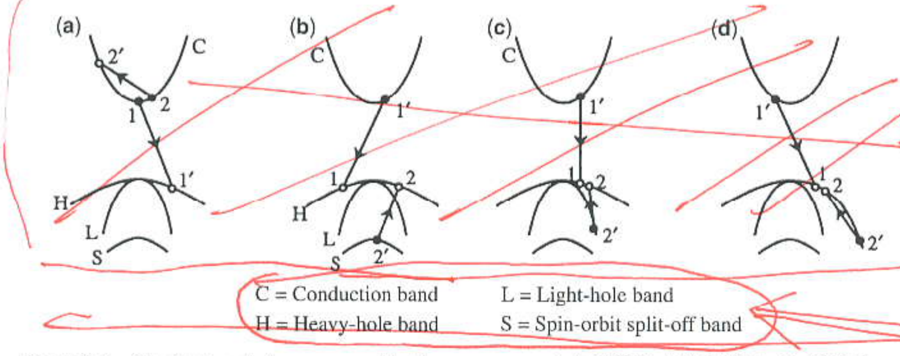

Figure 2.7 Band-to-band Auger recombination processes. (a) CHCC, (b) CHSH, (c) CHLH, and (d) CHHH processes.

Use Revised Fig. 2.7

Keep these 2 lines

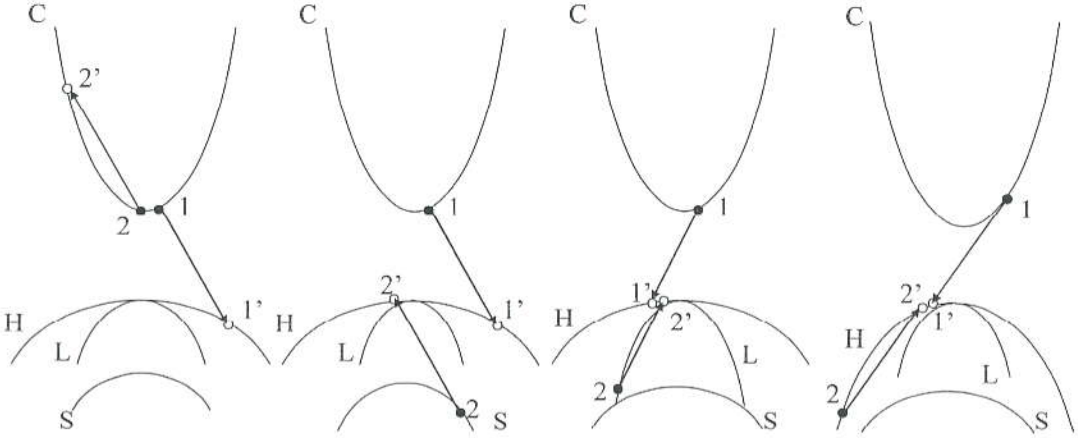

(a) CHCC process (b) CHSH process (c) CHLH process (d) CHHH process

New
Revised
Figure 2.7

where the carrier lifetime is

$$\tau(n) = (A + Bn + Cn^2)^{-1}. \tag{2.3.21}$$

Often, we define the radiative and radiative lifetimes: non

$$\tau_{\mathrm{r}} = \frac{1}{Bn} \qquad \tau_{\mathrm{nr}} = \frac{1}{A + Cn^2}. \tag{2.3.22}$$

The intrinsic quantum efficiency is the ratio of the radiative recombination rate to the total recombination rate

$$\eta_{\mathrm{in}} = \frac{1/\tau_{\mathrm{r}}}{1/\tau_{\mathrm{r}} + 1/\tau_{\mathrm{nr}}} = \frac{\tau_{\mathrm{nr}}}{\tau_{\mathrm{r}} + \tau_{\mathrm{nr}}}, \tag{2.3.23}$$

which is an important parameter for LEDs. Under a forward bias of a LED, the current injection determines the carrier density; therefore, the radiative recombination due to the spontaneous emission of photons (Bn^2) and the nonradiative recombinations ($An + Cn^3$).

2.3.4 Recombination by the Stimulated Emission Process

In semiconductor lasers and LEDs, stimulated emission of photons by incident photons causes recombination of electron–hole pairs, as shown in Fig. 1.4b. This recombination rate is given by the photon density S multiplied by the rate of growth, or group velocity (v_{g}) times gain coefficient $g(n)$

$$R = v_{\mathrm{g}} g(n) S. \tag{2.3.24}$$

The stimulated rate plays an important process in semiconductor lasers and will be used again in Chapter 10 for the analysis of semiconductor lasers to predict the light output power versus the injection current. It is also useful to predict the bandwidth of a directly modulated semiconductor laser when the injection current is modulated by an ac signal above threshold.

2.3.5 Impact Ionization Generation–Recombination Process [6]

This process is very much the same as the reverse Auger processes discussed above. However, the hot electron impact ionization processes usually depend on the incident current densities instead of the carrier concentrations. Microscopically, the processes are identical to the Auger-generation processes 2 and 4, which create an electron–hole pair due to an incident energetic electron or hole. These rates are usually given by

$$G_n = \alpha_n \frac{|J_n|}{q} \qquad G_p = \beta_p \frac{|J_p|}{q} \tag{2.3.25}$$

It is usually assumed that the quasi-Fermi levels stay as constants across the depletion region, that is, $F_N(x) = F_N$ for $-x_p \leq x < +\infty$, and $F_p(x) = F_p$ for $-\infty < x < x_N$, as shown in Fig. 2.14. This is equivalent to the statement that the carrier distribution in energy for the same species of carrier across the depletion region stays the same in the depletion region. As a result of this assumption, we find that, for the Boltzmann distribution, on the p-side

$$p_p(x) = N_{vp} e^{(E_v(x) - F_p(x))/k_B T} \tag{2.5.27a}$$

$$n_p(x) = N_{cp} e^{(F_N(x) - E_c(x))/k_B T}. \tag{2.5.27b}$$

On the N-side

$$P_N(x) = N_{VN} e^{(E_v(x) - F_p(x))/k_B T} \tag{2.5.28a}$$

$$N_N(x) = N_{CN} e^{(F_N(x) - E_c(x))/k_B T}. \tag{2.5.28b}$$

Because at thermal equilibrium (i.e., no current injection, $V = 0$), $F_p(x) = F_N(x)$

$$n_p p_p = N_{Vp} N_{cp} e^{-(E_c - E_v)/k_B T} = n_{ip}^2 \tag{2.5.29}$$

where n_{ip} is the intrinsic carrier concentration on the p-side. Thus, if $V \neq 0$, for $-x_p < x < 0$,

$$n_p p_p = n_{ip}^2 e^{(F_N - F_p)/k_B T} = n_{ip}^2 e^{qV/k_B T}. \tag{2.5.30}$$

At the edge of the depletion region, $x = -x_p$, $p_p(-x_p) \simeq p_{p0} \simeq N_a$. Therefore,

$$n_p(-x_p) \simeq \frac{n_{ip}^2}{N_a} e^{qV/k_B T} = n_{p0} e^{qV/k_B T}. \tag{2.5.31}$$

Here the subscript "0" in p_{p0} and n_{p0} refers to their thermal equilibrium values. The minority carrier near the edge of the depletion region, $n_p(-x_p)$, differs by a factor $\exp(qV/k_B T)$ from its thermal equilibrium value n_{p0} due to the carrier injection. Similarly, at the edge of the depletion region on the N-side, $x = x_N$, the minority carrier concentration is

$P_N(x_N)$

$$\overbrace{\underset{N}{P}(\underset{N}{x})} = P_{N0} e^{qV/k_B T} \tag{2.5.32}$$

where $P_{N0} = n_{iN}^2 / N_D$, where n_{iN} is the intrinsic carrier concentration on the N-side.

For the forward bias case, $V > 0$, when $\exp(qV/k_BT) \gg 1$, the above results in (2.5.47) and (2.5.48) can be further simplified and the quasi-Fermi levels are plotted in Fig. 2.14a. Similarly, for the reverse bias, $\exp(qV/k_BT) \ll 1$, the quasi-Fermi levels are plotted in Fig. 2.14b.

2.5.4 Current Densities and *I–V* Characteristics

The current densities are obtained for the minority carriers first. On the *p*-side, $J_n = qD_n \dfrac{\partial}{\partial x}\,\delta n(x)$, and on the *N*-side, $J_P \simeq -qD_P \dfrac{\partial}{\partial x}\,\delta P(x)$. Assuming that there is no generation or recombination current in the space charge region, that is, J_n and J_P are constant over the space charge region, the total current density is thus the

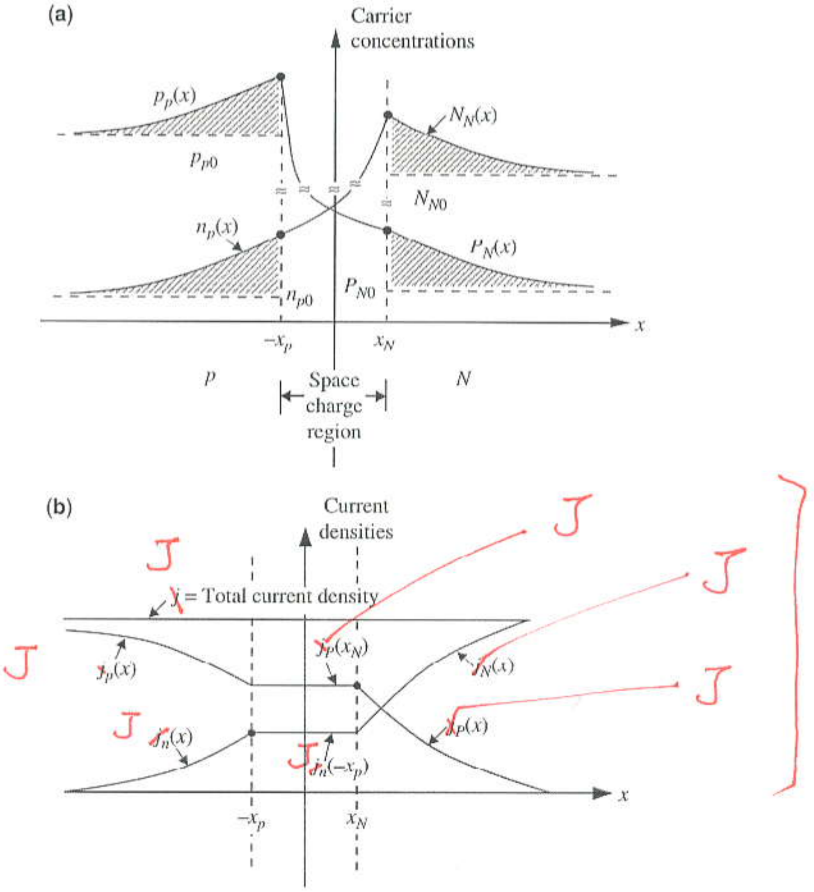

Figure 2.15 (a) The carrier concentrations and (b) the current densities as functions of position x in a forward biased *p-N* heterojunction diode using the depletion approximation.

chang all small j to Big J

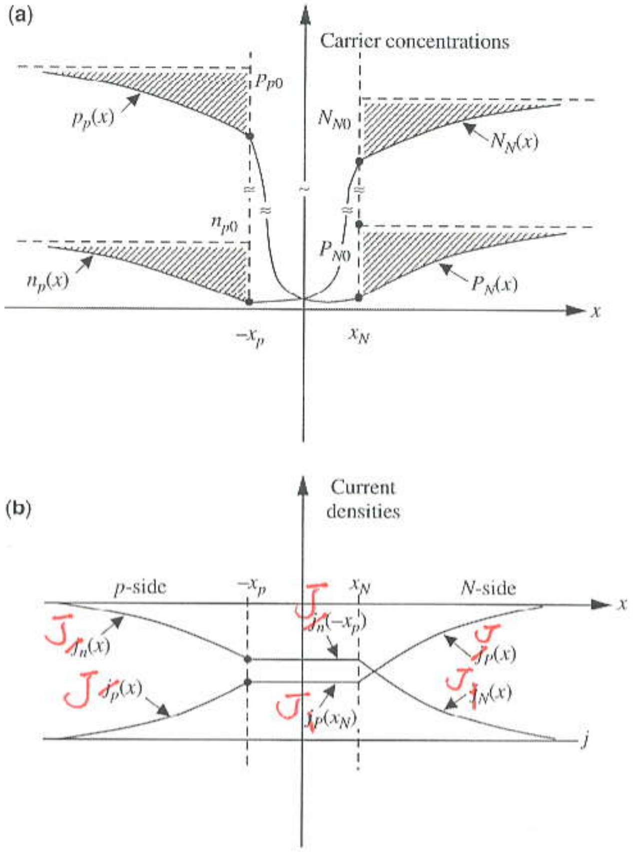

small j's to BIG J

Figure 2.16 (a) The carrier concentrations and (b) the current densities as functions of x for a reverse biased p-N heterojunction diode using the depletion approximation.

sum of the two current densities

$$\begin{aligned} J &= J_n(-x_p) + J_P(x_N) \\ &= q\left(\frac{D_n}{L_n}n_{p0} + \frac{D_P}{L_P}P_{N0}\right)(e^{qV/k_BT} - 1). \end{aligned} \qquad (2.5.50)$$

The total current is $I = jA$ with A the cross-sectional area of the diode.

$$I = I_0(e^{qV/k_BT} - 1) \qquad (2.5.51a)$$

$$I_0 = q\left(\frac{D_n}{L_n}n_{p0} + \frac{D_P}{L_P}P_{N0}\right)A. \qquad (2.5.51b)$$

and the probability current density as

$$\mathbf{j}(\mathbf{r}, t) = \frac{\hbar}{2mi}[\Psi^* \nabla \Psi - \Psi \nabla \Psi^*] \tag{3.1.6}$$

Here $\Psi^*(\mathbf{r},t)\Psi(\mathbf{r},t)d^3\mathbf{r}$ is the probability of finding the particle in a volume $d^3\mathbf{r}$ near the position $\mathbf{r}$ at time t. The wave function is normalized such that $\int \Psi^*(\mathbf{r}, t)\Psi(\mathbf{r}, t)d^3\mathbf{r} = 1$, that is, the probability of finding the particle in the whole space is unity. By substitution, it is straightforward to show that

$$\nabla \cdot \mathbf{j} + \frac{\partial}{\partial t}\rho = 0 \tag{3.1.7}$$

which is the continuity equation or the conservation of probability density. It is analogous to the charge continuity equation in electromagnetics.

The expectation value of any physical quantity defined by an operator O is given by

$$\langle O \rangle = \int_V \Psi^*(\mathbf{r}, t) O \Psi(\mathbf{r}, t) d^3\mathbf{r} = \langle \Psi | O | \Psi \rangle \tag{3.1.8}$$

where the volume of integration is over the whole space. The ket and bra vector, $|\Psi\rangle$ and $\langle\Psi|$, are used as short-hand notation. In the above real-space representation, that is, $\cancel{\psi} = \cancel{\psi}(\mathbf{r}, t)$, the correspondence for the operators is

Ψ

Ψ

(B/G)

$$\text{Position: } \mathbf{r}_{\text{op}} = \mathbf{r} \qquad \text{Momentum: } \mathbf{p}_{\text{op}} = \frac{\hbar}{i}\nabla. \tag{3.1.9}$$

If $V(\mathbf{r}, t)$ is independent of t, the solution $\Psi(\mathbf{r}, t)$ can always be obtained using the separation of variables

$$\Psi(\mathbf{r}, t) = \Psi(\mathbf{r})e^{-iEt/\hbar} \tag{3.1.10}$$

and

$$\left[-\frac{\hbar^2}{2m}\nabla^2 + V(\mathbf{r})\right]\Psi(\mathbf{r}) = E\Psi(\mathbf{r}) \tag{3.1.11}$$

which is the so-called time-independent Schrödinger equation. The solution may be in terms of quantized energy levels E_n with corresponding wave functions $\psi_n(\mathbf{r})$ or a continuous spectrum E with corresponding wave functions $\psi_E(\mathbf{r})$. In general, any solution of the Schrödinger equation may be constructed from the superposition of these stationary solutions

$$\Psi(\mathbf{r}, t) = \sum_n a_n \psi_n(\mathbf{r})e^{-iE_n t/\hbar} + \int_E a_E \psi_E(\mathbf{r})e^{-iEt/\hbar}\, dE \tag{3.1.12}$$

E

where $|a_n|^2$ gives the probability that the particle will be in the nth stationary (bound) state $\psi_n(\mathbf{r}, t)$ with an energy E_n, and a_E satisfies the normalization condition for the continuum states. In studying a time-dependent potential problem, very often a perturbation approach is used if the time-dependent perturbing potential is small compared with the unperturbed Hamiltonian, and the above expansion in terms of the stationary states $\psi_n(\mathbf{r})$ or $\psi_E(\mathbf{r})$, which are solutions to the unperturbed problem, is very useful. In this case, a_n (and a_E) will be functions of time as the perturbation is time-dependent, and $|a_n(t)|^2$ will give the time-dependent probability that the particle is in state n of the unperturbed problem.

If we write the Fourier transforms of $\psi(\mathbf{r})$ and $V(\mathbf{r})$ in the single-particle Schrödinger equation (3.1.11),

$$\tilde{\psi}(\mathbf{k}) = \int \psi(\mathbf{r}) e^{\ i\mathbf{k}\cdot\mathbf{r}} d^3\mathbf{r} \tag{3.1.13}$$

$$\tilde{V}(\mathbf{k}) = \int V(\mathbf{r}) e^{-i\mathbf{k}\cdot\mathbf{r}} d^3\mathbf{r} \tag{3.1.14}$$

we then obtain the momentum-space representation of the Schrödinger equation

$$\frac{\hbar^2 k^2}{2m}\tilde{\psi}(\mathbf{k}) + \int \frac{d^3\mathbf{k}'}{(2\pi)3\checkmark}\tilde{V}(\mathbf{k}-\mathbf{k}')\tilde{\psi}(\mathbf{k}') = E\tilde{\psi}(\mathbf{k}) \tag{3.1.15}$$

← superscript
3

which becomes an integral equation. This integral equation will be discussed in Chapter 14.

3.2 THE SQUARE WELL

We consider a square (or rectangular) quantum well with a barrier height V_0. In the one-dimensional case, the time-independent Schrödinger equation is

$$\left[-\frac{\hbar^2}{2m}\frac{d^2}{dz^2} + V(z)\right]\phi(z) = E\phi(z) \tag{3.2.1}$$

3.2.1 Infinite Barrier Model

First we assume V_0 is infinitely high; thus, the wave function vanishes at the boundaries, Fig. 3.1a. The solution to the infinite barrier model satisfying the boundary conditions $\phi_n(0) = 0$ and $\phi_n(L) = 0$ is

$$\phi_n(z) = \sqrt{\frac{2}{L}}\sin\left(\frac{n\pi}{L}z\right), \qquad n = 1, 2, 3, \ldots, \tag{3.2.2}$$

where we have used the polar coordinates,

$$dk_x dk_y = k_t d\phi dk_t, \quad k_t^2 = k_x^2 + k_y^2, \quad dE = \hbar^2 k_t dk_t / m^*.$$

We can then write the 2D density of states as

$$\rho_{2D}(E) = \frac{m^*}{\pi \hbar^2 L_z} \sum_n H(E - E_n) \tag{3.2.10}$$

where $H(x)$ is a Heaviside step function $H(x) = 1$ for $x > 0$ and $H(x) = 0$ for $x < 0$. The electron density n is then given by

$$n = \int dE \rho_{2D}(E) f(E). \tag{3.2.11}$$

The density of states $\rho_{2D}(E)$ is plotted in Fig. 3.2 as the steplike function with each step occurs wherever there is a new subband energy level E_1, $E_2 = 4E_1$, $E_3 = 9E_1$, and so forth. It is interesting to compare the two-dimensional density of states with the three-dimensional density of states (2.2.36)

$$\rho_{3D}(E) = \frac{1}{2\pi^2} \left(\frac{2m^*}{\hbar^2} \right)^{3/2} \sqrt{E}. \tag{3.2.12}$$

At $E = E_n$ from (3.2.3)

$$\begin{aligned} \rho_{3D}(E) &= \frac{1}{2\pi^2} \left(\frac{2m^*}{\hbar^2} \right)^{3/2} \left(\frac{\hbar^2 n^2 \pi^2}{2m^* L_z^2} \right)^{1/2} \\ &= n \left(\frac{m^*}{\pi \hbar^2 L_z} \right) \end{aligned} \tag{3.2.13}$$

← superscript ½

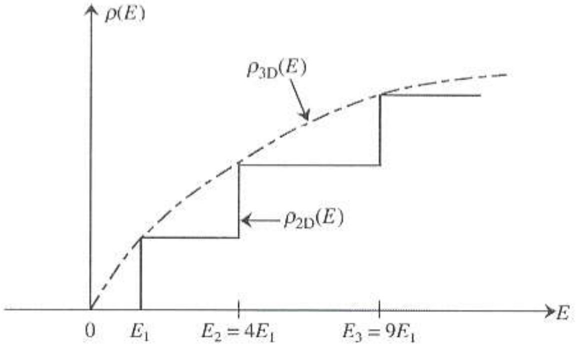

Figure 3.2 The electron density of states $\rho_{2D}(E)$ (solid line) for a two-dimensional quantum-well structure is compared with the three-dimensional density of states $\rho_{3D}(E)$ (dashed curve).

3.4 THE HYDROGEN ATOM AND EXCITON IN 2D AND 3D

In this section, we summarize the major results of the energies and wave functions for the hydrogen atom model with both bound ($E < 0$) and continuum ($E > 0$) state solutions [4–8]. The hydrogen atom is a two-particle system for the positive nucleus (with a mass m_1) at a position $\mathbf{r}_1$ and an electron (with mass m_2) at a position $\mathbf{r}_2$. The two-particle system is described by a wave function $\psi(\mathbf{r}_1, \mathbf{r}_2, t)$, which is a solution from the Hamiltonian

$$H = \frac{\mathbf{p}_1^2}{2m_1} + \frac{\mathbf{p}_2^2}{2m_2} + V(\mathbf{r}_1 - \mathbf{r}_2) \tag{3.4.1}$$

where $\mathbf{p}_1 = (\hbar/i)\nabla_1$ and $\mathbf{p}_2 = (\hbar/i)\nabla_2$, and ∇_i refers to the gradient operator with respect to $\mathbf{r}_i$ ($i = 1, 2$). A general solution is to transform from $\mathbf{r}_1$ and $\mathbf{r}_2$ coordinates to the center-of-mass coordinate $\mathbf{R}$,

$$\mathbf{R} = \frac{m_1\mathbf{r}_1 + m_2\mathbf{r}_2}{m_1 + m_2} \tag{3.4.2a}$$

and the difference coordinate $\mathbf{r}$,

$$\mathbf{r} = \mathbf{r}_1 - \mathbf{r}_2. \tag{3.4.2b}$$

The complete solution is of the form

$$\psi(\mathbf{r}_1, \mathbf{r}_2) = \frac{e^{i\mathbf{k}\cdot\mathbf{r}}}{\sqrt{V}}\psi(\mathbf{r}) \tag{3.4.3}$$

where $\psi(\mathbf{r})$ satisfies

$$\left[-\frac{\hbar^2}{2m_r}\nabla_r^2 - \frac{e^2}{4\pi\varepsilon r}\right]\psi(\mathbf{r}) = E\psi(\mathbf{r}) \tag{3.4.4}$$

where m_r is the reduced effective mass, $1/m_r = 1/m_1 + 1/m_2$.

3.4.1 3D Solutions

In three-dimensional space, the eigenfunctions can be expressed as

$$\cancel{\Psi}(\mathbf{r}) = \begin{cases} R_{nl}(r)\,Y_{lm}(\theta,\ \phi): & \text{bound-states } (E < 0) \\ R_{El}(r)\,Y_{lm}(\theta,\ \phi): & \text{continuum-states } (E < 0) \end{cases} \tag{3.4.5}$$

ψ (italic) (small)

where the radial functions $R_{nl}(r)$ and $R_{El}(r)$ can be found in Refs. 4–8 and 10. The first few spherical harmonics $Y_{lm}(\theta, \phi)$ are given as follows:

$l = 0$ (s orbit)

$$Y_{00} = \frac{1}{\sqrt{4\pi}} \tag{3.4.6}$$

3.4.2 2D Solutions

The solutions for the two-dimensional hydrogen atom problem are given by

ψ (italic) small

$$\cancel{\Psi}(\mathbf{r}) = \begin{cases} R_{nm}(r)\dfrac{e^{im\phi}}{\sqrt{2\pi}}, & \text{bound-states } (E < 0) \\ R_{Em}(r)\dfrac{e^{im\phi}}{\sqrt{2\pi}}, & \text{continuum-states } (E > 0). \end{cases} \tag{3.4.13}$$

The eigenenergies for the bound states are quantized

$$E_n = -\frac{R_y}{\left(n - \dfrac{1}{2}\right)^2} \quad (n = 1, 2, 3, \ldots). \tag{3.4.14}$$

We have

$$E_1 = -4R_y,\ E_2 = -\frac{4}{9}R_y,\ E_3 = -\frac{4}{25}R_y, \ldots \tag{3.4.15}$$

It is noted that the binding energy for the 1s states $|E_1|$ is four times that in the three-dimensional case. This enhancement of the binding energy will be very useful in understanding the excitonic effects in semiconductor quantum wells and the observation of the excitonic optical absorption spectra, which will be investigated in Chapter 14. The wavefunction at the origin is

$$|\psi_{n0}(\mathbf{r} = 0)|^2 = \frac{1}{\pi a_0^3\left(n - \dfrac{1}{2}\right)^3} \quad (n = 1, 2, 3, \ldots). \tag{3.4.16}$$

For continuum states, the energy E is a continuous variable, and the wave function at the origin is

$$|\psi_{E0}(\mathbf{r} = 0)|^2 = \frac{1}{R_y a_0^3 4\pi}\left[\frac{e^{\pi/(ka_0)}}{\cosh\left(\dfrac{\pi}{ka_0}\right)}\right] \tag{3.4.17}$$

where $E = \hbar^2 k^2/2m_r$. The expression inside the square bracket is the Sommerfeld enhancement factor.

3.5 TIME-INDEPENDENT PERTURBATION THEORY

3.5.1 Perturbation Method

In most practical physical systems, the Schrödinger equations do not have exact or analytical solutions. It is always convenient to find the solutions using the

(b) If we keep only the first two nonvanishing terms in the above summation for C_n, we obtain

$$C_1 = \frac{32}{\pi^6} \times \left[\frac{4\times 2^2}{(1-2^2)^5} + \frac{4\times 4^2}{(1^2-4^2)^5}\right] = -2.194\times 10^{-3}$$

$$C_2 = \frac{32\times 2^2}{\pi^6} \times \left[\frac{4\times 1^2}{(4-1)^5} + \frac{4\times 3^2}{(4-9)^5}\right] = 6.578\times 10^{-4}$$

$$C_3 = \frac{32\times 3^2}{\pi^6} \times \left[\frac{4\times 2^2}{(9-4)^5} + \frac{4\times 4^2}{(9-16)^5}\right] = 3.931\times 10^{-4}.$$

We see that E_1 decreases with increasing field F as $C_1 < 0$ and both E_2 and E_3 increase slightly with increasing field F.

(c) The above C_n in part (a) can be summed up to an analytical expression [12–14]

Superscript 4

$$C_n = \frac{n^2\pi^2 - 15}{24n^4\pi^{\cancel{5}}} \quad \text{or} \quad C_1 = -2.194\times 10^{-3}, \quad C_2 = 6.544\times 10^{-4}, \text{ and}$$

4

$$C_3 = 3.899\times 10^{-4}$$

which are close to those in (b). These results using the second-order perturbation theory agree very well with those obtained from variational methods [14–17].

3.5.2 Matrix Formulation

Alternatively, the eigenvalue problem

$$H\psi = \left(H^{(0)} + H'\right)\psi = E\psi \tag{3.5.30}$$

can be solved directly by letting

$$\psi = \sum_m a_m \phi_m^{(0)} \tag{3.5.31}$$

where $\{\phi_m^{(0)}\}$ are the eigenfunctions of the unperturbed Hamiltonian,

$$H_0\phi_m^{(0)} = E_m^{(0)}\phi_m^{(0)}. \tag{3.5.32}$$

The second subscript n in a is dropped for convenience. Here $\phi_m^{(0)}, m = 1, 2, \ldots, N$, may also be degenerate wave functions. A direct substitution of (3.5.31) into (3.5.30), and taking the inner product with respect to $\phi_k^{(0)}, k = 1, \ldots, N$, gives

$$\sum_m (H_{km} - E\delta_{km})a_m = 0 \tag{3.5.33}$$

The Kane's parameter P can also be related to the effective mass of the electron m_e^* using

$$E_c(k) - E_g = \frac{\hbar^2 k^2}{2m_0} + \frac{k^2 P^2\left(E_g + \frac{2}{3}\Delta\right)}{E_g(E_g + \Delta)} = \frac{\hbar^2 k^2}{2m_e^*} \tag{4.2.25}$$

$$P^2 = \left(1 - \frac{m_e^*}{m_0}\right)\frac{\hbar^2 E_g(E_g+\Delta)}{2m_e^*\left(E_g + \frac{2\Delta}{3}\right)}. \tag{4.2.26}$$

Sometimes, the $\hbar^2 k^2/2m_0$ term is ignored, as $m_e^* \simeq 0.067m_0 \ll m_0$ for GaAs; therefore, the term m_e^*/m_0 in (4.2.26) is ignored.

We note that these wave functions in (4.2.21)–(4.2.24) are eigenvectors of the Hamiltonian

$$H = H_0 + \frac{\hbar^2 k^2}{2m_0} + \frac{\hbar}{m_0}\mathbf{k}\cdot\mathbf{p} + \frac{\hbar}{4m_0^2c^2}\sigma\cdot\nabla V\times\mathbf{p} \tag{4.2.27}$$

with eigenenergies $E = E_g, 0, 0, -\Delta$ as $k \longrightarrow 0$ for the conduction, heavy-hole, light-hole, and spin split-off bands, respectively.

4.2.5 General Coordinate Direction

If k is not along the z-direction,

$$\mathbf{k} = k\sin\theta\cos\varphi\hat{x} + k\sin\theta\sin\varphi\hat{y} + k\cos\theta\,\hat{z} \tag{4.2.28}$$

the following transformations can be used to find the basis functions in the general coordinate system

$$\begin{bmatrix}\uparrow'\\ \downarrow'\end{bmatrix} = \begin{pmatrix} e^{-i\phi/2}\cos\frac{\theta}{2} & e^{i\phi/2}\sin\frac{\theta}{2}\\ -e^{-i\phi/2}\sin\frac{\theta}{2} & e^{i\phi/2}\cos\frac{\theta}{2}\end{pmatrix}\begin{bmatrix}\uparrow\\ \downarrow\end{bmatrix} \tag{4.2.29}$$

$$\begin{bmatrix}X'\\ Y'\\ Z'\end{bmatrix} = \begin{bmatrix}\cos\theta\cos\phi & \cos\theta\overset{\text{sin}}{\cancel{\cos}}\phi & -\sin\theta\\ -\sin\phi & \cos\phi & 0\\ \sin\theta\cos\phi & \sin\theta\underset{\text{sin}}{\cancel{\cos}}\phi & \cos\theta\end{bmatrix}\begin{bmatrix}X\\ Y\\ Z\end{bmatrix}. \tag{4.2.30}$$

← sin

← sin

The spherically symmetrical function maintains its symmetry, $S(r') = S(r)$ as $r' = r$ because the length scale is preserved in a unitary transformation. The above transformation will be useful in Chapter 9 when we discuss optical matrix elements for quantum wells.

Dot-multiplying (5.2.1) by $\mathbf{H}$ and (5.2.2) by $\mathbf{E}$, and taking the difference, we obtain

$$\nabla \cdot (\mathbf{E} \times \mathbf{H}) = -\mathbf{H} \cdot \frac{\partial}{\partial t}\mathbf{B} - \mathbf{E} \cdot \frac{\partial \mathbf{D}}{\partial t} - \mathbf{E} \cdot \mathbf{J} \tag{5.2.3}$$

where $\nabla \cdot (\mathbf{E} \times \mathbf{H}) = \mathbf{H} \cdot \nabla \times \mathbf{E} - \mathbf{E} \cdot \nabla \times \mathbf{H}$ has been used. Define the Poynting vector as

$$\mathbf{S} = \mathbf{E} \times \mathbf{H} \tag{5.2.4}$$

which gives the energy flux density (W/m^2). For an isotropic medium, $\mathbf{D} = \varepsilon \mathbf{E}$ and $\mathbf{B} = \mu \mathbf{H}$, the electric and magnetic energy densities are

$$\begin{aligned} w_{\mathrm{e}} &= \frac{\varepsilon}{2}\mathbf{E} \cdot \mathbf{E} \\ w_{\mathrm{m}} &= \frac{\mu}{2}\mathbf{H} \cdot \mathbf{H}. \end{aligned} \tag{5.2.5}$$

Therefore, Poynting's theorem in the time domain is simply

$$\nabla \cdot \mathbf{S} = -\frac{\partial}{\partial t}(w_{\mathrm{e}} + w_{\mathrm{m}}) - \mathbf{E} \cdot \mathbf{J}. \tag{5.2.6}$$

The theorem simply states the power flow, or the divergence of the power density $\mathbf{S}$, is given by the decreasing rate of the total electric and magnetic energy density plus the power generated by the current source, $-\mathbf{E} \cdot \mathbf{J}$. If integrating over a volume V enclosed by a surface S, we obtain Poynting's theorem in the form

$$\iint_S \mathbf{E} \times \mathbf{H} \cdot d\mathbf{S} = -\frac{\partial}{\partial t}\iiint_V (w_{\mathrm{e}} + w_{\mathrm{m}})\, dV - \iiint_V \mathbf{E} \cdot \mathbf{J}\, dV \tag{5.2.7}$$

that is, the power flow out of the surface S equals the decreasing rate of the stored electric and magnetic energies plus the power supplied by the source, $-\iiint \mathbf{E} \cdot \mathbf{J}\, dV$.

A complex Poynting's theorem can also be derived from Maxwell's equations in frequency domain

Insert $\frac{1}{2}$

$$\frac{1}{2}\nabla \cdot (\mathbf{E} \times \mathbf{H}^*) = -i\omega\left(\frac{1}{2}\mathbf{E} \cdot \mathbf{D}^* - \frac{1}{2}\mathbf{B} \cdot \mathbf{H}^*\right) - \frac{1}{2}\mathbf{E} \cdot \mathbf{J}^*. \tag{5.2.8}$$

If $\mathbf{J} = \mathbf{J}_{\mathrm{d}} + \mathbf{J}_{\mathrm{f}}$ where $\mathbf{J}_{\mathrm{d}}$ accounts for dissipation (e.g., $\mathbf{J}_{\mathrm{d}} = \sigma \mathbf{E}$ in a conductor), we then have

$$\frac{1}{2}\nabla \cdot (\mathbf{E} \times \mathbf{H}^*) + i\frac{\omega}{2}(\mathbf{E} \cdot \mathbf{D}^* - \mathbf{B} \cdot \mathbf{H}^*) + \frac{1}{2}\mathbf{E} \cdot \mathbf{J}_{\mathrm{d}}^* = \frac{-1}{2}\mathbf{E} \cdot \mathbf{J}_{\mathrm{f}}^*. \tag{5.2.9}$$

where λ is the wavelength in free space. For a plane wave propagating in the $+z$-direction with a polarization along $\hat{x}$, the electric field behaves as follows:

$$\mathbf{E} = \hat{x}\, E_0\, e^{ikz} = \hat{x}\, E_0 \exp\left(i\frac{2\pi}{\lambda} nz - \frac{\alpha}{2} z \right) \tag{5.5.7a}$$

$$\mathbf{H} = \hat{y}\, \frac{E_0}{\eta}\, e^{ikz} = \hat{y}\, \frac{\bar{n} E_0}{\eta_0} \exp\left(i\frac{2\pi}{\lambda} nz - \frac{\alpha}{2} z \right), \tag{5.5.7b}$$

where $\eta_0 = \sqrt{\mu_0/\varepsilon_0} = 120\pi$ is the characteristic impedance of the free space. The time-averaged Poynting vector for the optical power density is

$$\mathbf{S} = \frac{1}{2} \mathrm{Re}[\mathbf{E} \times \mathbf{H}^*] = \hat{z}\, \frac{n}{2\eta_0} |E_0|^2\, e^{-\alpha z} \tag{5.5.8}$$

which decays exponentially as the wave propagates farther along the z-direction with a decay constant determined by the absorption coefficient.

5.5.2 Lorentz Dipole Model

In a resonant dielectric medium such as a collection of resonant atoms in the presence of a driving electromagnetic field $E(t)$, we can model each resonant atom as a classic harmonic oscillator, Fig. 5.2. The equation ~~is~~ motion is determined by the reduced mass for a free electron with mass m_0 bound to a nucleus with mass M [6–8]

of

$$\frac{1}{m_r} = \frac{1}{m_0} + \frac{1}{M}. \tag{5.5.9}$$

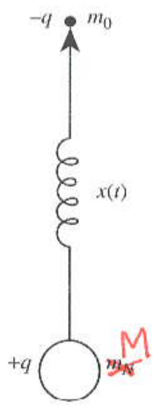

Big
← M

Figure 5.2 A classic dipole oscillator model for an electron bound to a positive nucleus. The resonant frequency $\omega_0 = \sqrt{k/m_r}$ is characterized by the restoring spring constant k and the reduced mass m_r.

Usually, $M \gg m_0$, therefore, $m_r \approx m_0$. The equation of motion for the displacement of the electron with a unit charge $-q$ from its equilibrium position is governed by

$$m_0 \frac{d^2x}{\partial t^2} + m_0\gamma\frac{dx}{dt} + kx = -qE(t) \tag{5.5.10}$$

where γ is a damping factor and k is the spring constant. For a time harmonic optical electromagnetic field, $E(t) = E_0 e^{-i\omega t}$, the dipole moment of the electron $-q$ and the positive nucleus $+q$ is given by

$$p = -qx(t) = \frac{q^2E(t)}{m_0(-\omega^2 \cancel{+} i\gamma\omega + \omega_0^2)} \tag{5.5.11}$$

— (minus)

where a resonant frequency $\omega_0 - \sqrt{k/m_0}$ has been defined. The polarization density P due to N atoms or electron–nucleus pairs per unit volume (1/cm^3) is

$$P = Np = \frac{Nq^2E(t)}{m_0(-\omega^2 - i\gamma\omega + \omega_0^2)}. \tag{5.5.12}$$

The displacement vector D is given by

$$\begin{aligned} D &= \varepsilon_0 E + P_b + P \\ &= \varepsilon_0\left[1 + \chi_b + \frac{Nq^2}{m_0\varepsilon_0(\omega_0^2 - \omega^2 - i\gamma\omega)}\right]E \end{aligned} \tag{5.5.13}$$

where we have included the background contribution to the polarization density $P_b = \varepsilon_0\chi_b E$. We obtain the permittivity function for the resonant dielectric medium or an atomic gas:

$$\varepsilon(\omega) = \varepsilon_0[1 + \chi_b + \chi(\omega)] \tag{5.5.14a}$$

$$\chi(\omega) = \frac{Nq^2}{m_0\varepsilon_0(\omega_0^2 - \omega^2 - i\gamma\omega)} = \frac{\omega_p^2}{(\omega_0^2 - \omega^2 - i\gamma\omega)} \tag{5.5.14b}$$

where

$$\omega_p = \sqrt{\frac{Nq^2}{m_0\varepsilon_0}} \tag{5.5.15}$$

is the plasma frequency. Separating the real and imaginary parts, $\chi = \chi' + i\chi''$,

← ,

$$\chi'(\omega) = \frac{\omega_p^2(\omega_0^2 - \omega^2)}{(\omega_0^2 - \omega^2)^2 + (\gamma\omega)^2} \tag{5.5.16a}$$

$$\chi''(\omega) = \frac{\omega_p^2\gamma\omega}{(\omega_0^2 - \omega^2)^2 + (\gamma\omega)^2}. \tag{5.5.16b}$$

The relative permittivity or dielectric function is given by

$$\begin{aligned} \varepsilon_{\mathrm{r}}(\omega) &= \frac{\varepsilon(\omega)}{\varepsilon_0} = \varepsilon_{\mathrm{r}}'(\omega) + i\varepsilon_{\mathrm{r}}''(\omega) \\ &= 1 + \chi_{\mathrm{b}} + \chi'(\omega) + i\chi''(\omega) \qquad (5.5.17\mathrm{a}) \\ \varepsilon_{\mathrm{r}}'(\omega) &= 1 + \chi_{\mathrm{b}} + \chi'(\omega) \qquad (5.5.17\mathrm{b}) \\ \varepsilon_{\mathrm{r}}''(\omega) &= \chi''(\omega). \qquad (5.5.17\mathrm{c}) \end{aligned}$$

We denote the static (dc) value of the permittivity at zero frequency,

$$\chi_{\mathrm{s}} = \chi(0) = \frac{\omega_{\mathrm{p}}^2}{\omega_0^2} \qquad (5.5.18\mathrm{a})$$

$$\varepsilon_{\mathrm{s}} = \varepsilon_{\mathrm{r}}(0) = 1 + \chi_{\mathrm{b}} + \chi_0. \qquad (5.5.18\mathrm{b})$$

The other limit as ω approaches infinity is $\chi(\infty) = 0$, that is, the medium polarization simply cannot respond to the fast varying driving electromagnetic field, and the dielectric constant in the high-frequency limit is given by the background value:

$$\varepsilon_\infty = \varepsilon_{\mathrm{r}}(\infty) = 1 + \chi_{\mathrm{b}}. \qquad (5.5.19)$$

Figure 5.3 plots the real and imaginary parts of the susceptibility χ. The imaginary part peaks at the resonant frequency ω_0 as expected, with a full-width at half maximum of γ. The plasma resonance is also given as

$$Q = \frac{\omega_0}{(\Delta\omega)_{\mathrm{FWHM}}} = \frac{\omega_0}{\gamma} \qquad \chi_{\mathrm{peak}}''(\omega_0) = \chi_0 Q. \qquad (5.5.20)$$

The real part has a zero crossing at the resonant frequency and is positive for frequency below resonance and is negative for frequency above resonance. The complex propagation constant is

$$\begin{aligned} k &= \omega\sqrt{\mu_0\varepsilon} = \omega\sqrt{\mu_0[\varepsilon_{\mathrm{b}} + \varepsilon_0\chi(\omega)]} \\ &\approx \omega\sqrt{\mu_0\varepsilon_{\mathrm{b}}}\left\{1 + \frac{\varepsilon_0}{2\varepsilon_{\mathrm{b}}}[\chi' + i\chi'']\right\} \\ &= k_0 n_{\mathrm{b}} + k_0\Delta n + i\frac{\alpha}{2} \qquad (5.5.21) \end{aligned}$$

where $n_{\mathrm{b}} = \sqrt{\varepsilon_{\mathrm{b}}/\varepsilon_0}$ is the background ~~dielectric constant~~ refractive index.

Here the approximation is valid only if the second term is much smaller than the first background permittivity. Otherwise, (5.5.4a) and (5.5.4b) have to be used. We have then,

$$\Delta n = \frac{1}{2n_{\mathrm{b}}}\chi' = \text{ the change in refractive index} \qquad (5.5.22\mathrm{a})$$

superscript

—

– (minus)

The transmitted fields are

$$\mathbf{E}_t = \hat{y} t E_0 e^{ik_{2x}x + ik_{2z}z} \tag{5.6.5a}$$

–

Delete

$$\mathbf{H}_t = \frac{-1}{\omega\mu_2}(\cancel{+}k_{2z}\hat{x} + k_{2x}\hat{z}) t E_0 e^{ik_{2x}x + ik_{2z}z} \tag{5.6.5b}$$

ℊ, —

/

where

$$k_{2x}^2 + k_{2z}^2 = \omega^2 \mu_2 \varepsilon_2 = k_0^2 n_2^2 \tag{5.6.6}$$

and $n_2 = \sqrt{\mu_2\varepsilon_2/\mu_0\varepsilon_0}$. Matching the boundary conditions in which the tangential electric field (E_y) is continuous at $x = 0$,

$$E_0 e^{ik_{1z}z} + r\, E_0 e^{ik_{1z}^r z} = t E_0 e^{ik_{2z}z} \tag{5.6.7}$$

for all z, we obtain

$$k_{1z} = k_{1z}^r = k_{2z} \tag{5.6.8}$$

$$1 + r = t. \tag{5.6.9}$$

Equation (5.6.8) is Snell's law or the phase-matching condition, Fig. 5.5b,

$$k_1 \sin\theta_i = k_1 \sin\theta_r = k_2 \sin\theta_t \tag{5.6.10}$$

or

$$\begin{aligned} \theta_i &= \theta_r \\ n_1 \sin\theta_i &= n_2 \sin\theta_t, \end{aligned} \tag{5.6.11}$$

where $k_i = \omega\sqrt{\mu_i\varepsilon_i} = k_0 n_i,\ \ i = 1, 2$. The other boundary condition in which the tangential magnetic field (H_z) is continuous leads to

$$1 - r = \frac{\mu_1\, k_{2x}}{\mu_2\, k_{1x}} t \tag{5.6.12}$$

Solving (5.6.9) and (5.6.12) for r and t, we obtain the reflection coefficient

$$r = \frac{1 - \left(\dfrac{\mu_1\, k_{2x}}{\mu_2\, k_{1x}}\right)}{1 + \left(\dfrac{\mu_1\, k_{2x}}{\mu_2\, k_{1x}}\right)} = \frac{n_1\cos\theta_i - n_2\cos\theta_t}{n_1\cos\theta_i + n_2\cos\theta_t} \tag{5.6.13}$$

and the transmission coefficient

$$t = \frac{2}{1 + \left(\dfrac{\mu_1\, k_{2x}}{\mu_2\, k_{1x}}\right)} = \frac{2n_1\cos\theta_i}{n_1\cos\theta_i + n_2\cos\theta_t} \tag{5.6.14}$$

Special Case for Normal Incidence At normal incidence, $\theta_i = 0°$, $k_{2x} = k_2 = k_0 n_2$ and $k_{1x} = k_1 = k_0 n_1$. We find the reflection and transmission coefficients for the field are, respectively,

$$r_{12} = \frac{n_1 - n_2}{n_1 + n_2} \qquad t_{12} = \frac{2n_1}{n_1 + n_2} \tag{5.6.21}$$

At an optical energy below the band gap of most semiconductors, the absorption is usually small or negligible. Above the band gap, the optical absorption is important. When a plane wave is normally incident from the air to a semiconductor surface, the reflectivity of the power is

$$R = \left|\frac{n_0 - \bar{n}}{n_0 + \bar{n}}\right|^2 = \frac{(n-1)^2 + \kappa^2}{(n+1)^2 + \kappa^2} \tag{5.6.22}$$

which takes into account the absorption effect when the refractive index $\bar{n}$ is complex and n_0 of the air is 1.

Numerical Example For InP material, the dispersive effects of the real and the imaginary parts $n(\omega)$ and $\kappa(\omega)$ are given in Appendix B at the end of the text as a function of the photon energy $\hbar\omega$ or the free-space wavelength λ. At an energy $\hbar\omega = 2.0\,\text{eV}$ ($\lambda = 0.62\,\mu\text{m}$), which is close to that of a HeNe laser wavelength, we have $n = 3.549$, and $\kappa = 0.317$. The absorption coefficient is

$$\alpha = \frac{4\pi}{\lambda}\kappa = \frac{4\pi}{0.62\,\mu\text{m}} \times 0.317 = 6.43 \times 10^4\,\text{cm}^{-1}.$$

The reflectivity for the reflected power from the semiconductor is

$$R = \frac{(3.549 - 1)^2 + 0.317^2}{(3.549 - 1)^2 + 0.317^2} = 0.31\overset{4}{\cancel{7}}.$$

0.314

+

5.6.2 TM Polarization

The result of TM polarization can be obtained by the duality principle using the exchange of the physical quantities in Section 5.6.1. The results are

$$\mathbf{H}_i = \hat{y}\,H_y = \hat{y}\,H_0 e^{-ik_{1x}x + ik_{1z}z} \tag{5.6.23a}$$

$$\mathbf{H}_r = \hat{y}\,r_{TM}\,H_0 e^{+ik_{1x}x + ik_{1z}z} \tag{5.6.23b}$$

$$\mathbf{H}_t = \hat{y} t_{TM}\,H_0 e^{-ik_{2x}x + ik_{2z}z} \tag{5.6.23c}$$

where $k_{2z} = k_{1z}$ and

$$r_{\mathrm{TM}} = \frac{1 - \left(\dfrac{\varepsilon_1 k_{2x}}{\varepsilon_2 k_{1x}}\right)}{1 + \left(\dfrac{\varepsilon_1 k_{2x}}{\varepsilon_2 k_{1x}}\right)} = \frac{n_2 \cos\theta_{\mathrm{i}} - n_1 \cos\theta_{\mathrm{t}}}{n_2 \cos\theta_{\mathrm{i}} + n_1 \cos\theta_{\mathrm{t}}} \tag{5.6.24a}$$

$$t_{\mathrm{TM}} = \frac{2}{1 + \left(\dfrac{\varepsilon_1 k_{2x}}{\varepsilon_2 k_{1x}}\right)} = \frac{2n_2 \cos\theta_{\mathrm{i}}}{n_2 \cos\theta_{\mathrm{i}} + n_1 \cos\theta_{\mathrm{t}}}. \tag{5.6.24b}$$

Brewster Angle For two dielectric media, the reflection coefficient for the TM polarized light vanishes when $\varepsilon_2 k_{1x} = \varepsilon_1 k_{2x}$, which means

$$n_2 \cos\theta_{\mathrm{i}} = n_1 \cos\theta_{\mathrm{t}}. \tag{5.6.25a}$$

Snell's law requires that

$$n_1 \sin\theta_{\mathrm{i}} = n_2 \sin\theta_{\mathrm{t}} \tag{5.6.25b}$$

The above two equations are satisfied if $\theta_{\mathrm{i}} + \theta_{\mathrm{t}} = 90^\circ$. This angle of incidence θ_{i} at which the reflection vanishes is called the Brewster angle θ_{B}

$$\theta_{\mathrm{B}} = \tan^{-1}(n_2/n_1). \tag{5.6.26}$$

Unlike the critical angle, $\theta_{\mathrm{c}} = \sin^{-1}(n_2/n_1)$, which requires $n_2 < n_1$, the Brewster angle exists for wave transmission in either direction.

from medium 1 to 2 or 2 to 1.

For total internal reflection, $k_{2x} = i\alpha_2$, and $r_{\mathrm{TM}} = e^{-i2\phi_{12}^{\mathrm{TM}}}$ where

$$\phi_{12}^{\mathrm{TM}} = \tan^{-1}\left(\frac{\varepsilon_1 \alpha_2}{\varepsilon_2 k_{1x}}\right). \tag{5.6.27}$$

The magnetic field experiences a Goos–Hänchen phase shift of an amount $-2\phi_{12}^{\mathrm{TM}}$ when the angle of incidence is larger than the critical angle θ_{c}.

Example Consider InP ($n = 3.16$) and air interface. We plot the reflectivity of power for TE and TM polarizations for plane wave reflection (a) from air to InP surface, and (b) from InP toward the air interface in Fig. 5.6a and Fig. 5.6b, respectively. For case (a), there is no total internal reflection. The reflectivity of the TE polarization is always larger than that of the TM polarization. The Brewster angle occurs at 72.4°. For case (b), total internal reflection occurs at 18.4°, beyond which both TE and TM polarized lights have a unity reflectivity. The Brewster angle occurs at 17.6°.

5.6.3 Concept of Impedance for Plane Wave Propagation

In free space, the ratio of the transverse electric and magnetic fields for a plane wave is simply $\eta_0 = \sqrt{\mu_0/\varepsilon_0} = 120\pi\Omega$. For a plane wave incident obliquely onto a surface

Similar relations between the real part and imaginary part of the complex refractive index, $\bar{n}(\omega) = n(\omega) + i\kappa(\omega)$ exist

$$n(\omega) - 1 = P\int_{-\infty}^{\infty} \frac{d\omega'}{\pi}\frac{\kappa(\omega)}{\omega' - \omega} \tag{5A.18}$$

$$\kappa(\omega) = -P\int_{-\infty}^{\infty} \frac{d\omega'}{\pi}\frac{n(\omega') - 1}{\omega' - \omega}. \tag{5A.19}$$

PROBLEMS

5.1 Check the duality principle using (5.1.12).

5.2 For a laser light with a power 1 mW propagating in a GaAs semiconductor ($n = 3.5$) waveguide with a cross section 10 μm × 1 μm, find **(a)** the power density if we assume the intensity is uniform with the waveguide cross section, **(b)** the electric field strength and the magnetic field strength assuming it is a uniform plane wave.

5.3 Derive (5.5.4a) and (5.5.4b).

5.4 Plot the real and imaginary parts of the relative permittivity using (5.5.32) for gold and check with Fig. 5.4.

5.5 **(a)** A plane wave is reflected between the free space and a bulk GaAs semiconductor with a refractive index assumed to be $n = 3.5$. Calculate the reflection and the transmission coefficients of the field, r and t, at normal incidence.

(b) Repeat part **(a)** if the wave is incident from the GaAs region onto the GaAs/air interface at normal incidence.

(c) For oblique incidence in part **(b)**, find the critical angle and the Brewster angle.

5.6 For a plane wave incident from an InP region ($n = 3.16$ and free space wavelength $\lambda = 1.55$ μm) to air ~~and reflected~~ with an angle of incidence $\theta_i = 15°$, calculate **(a)** the reflection and the transmission coefficients, r and t, of the optical field for both TE and TM polarizations, and **(b)** the reflectivity R and the transmissivity T for both polarizations.

5.7 Calculate the Goos–Hänchen phase shifts for an angle of incidence $\theta_i = 45°$ between an InP/air interface for both TE and TM polarizations ($n = 3.16$ and $\lambda = 1.55$ μm).

5.8 **(a)** Calculate the reflection and transmission coefficients, r and t, for a plane wave normally incident on a slab of GaAs sample with a thickness $d = 10$ μm and a refractive index $n = 3.5$ at a wavelength $\lambda = 1$ μm.

(b) Find the power reflectivity and transmissivity in part **(a)**.

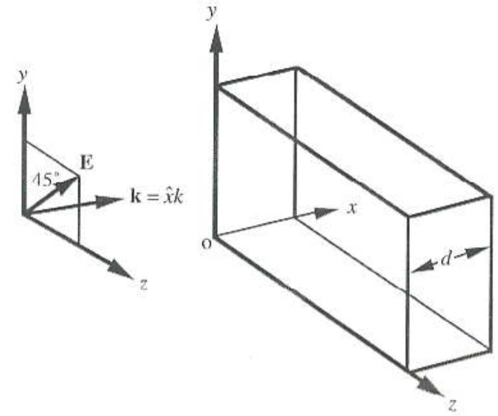

Figure 6.5 A plane wave **E** incident on a uniaxial medium with a thickness d. The electric field vector makes an angle of 45° with the two principal (y and z) axes.

we obtain

$$E = \left[\hat{y} + \hat{z}e^{i(k_e - k_o)d}\right]\frac{E_0}{\sqrt{2}}e^{ik_o d}$$

$$= (\hat{y} \pm i\hat{z})\frac{E_0}{\sqrt{2}}e^{ik_o d} \quad \text{for } (k_e - k_o)d = \begin{cases} \dfrac{\pi}{2}, & \dfrac{5\pi}{2}, \quad \dfrac{9\pi}{2}, \ldots \\[2ex] \dfrac{3\pi}{2}, & \dfrac{7\pi}{2}, \quad \dfrac{11\pi}{2}, \ldots \end{cases} \tag{6.1.36}$$

which becomes circularly polarized at the output end $x = d$. Using

$$k_e = \frac{2\pi}{\lambda_e} = \frac{\omega}{c}n_e \tag{6.1.37a}$$

$$k_o = \frac{2\pi}{\lambda_e} = \frac{\omega}{c}n_o \tag{6.1.37b}$$

subscript
o
as in "ordinary".

and defining

$$k_e - k_o = \frac{2\pi}{\lambda_d} \quad \text{or} \quad \lambda_d = \frac{\lambda}{|n_e - n_o|} \tag{6.1.37c}$$

where λ is the wavelength in free space ($\omega/c = 2\pi/\lambda$), we have

$$d = \frac{\lambda_d}{4}, \frac{3\lambda_d}{4}, \frac{5\lambda_d}{4}, \ldots \tag{6.1.38}$$

Thus the plate, which can transform an incident linearly polarized wave into a circularly polarized wave, is called a quarter-wave plate. Note that the value λ_d is neither the wavelength in the free space nor the wavelength in the uniaxial medium (it corresponds

>

subscripts

o as in

o "o"rdinary

o

<

o

with 2π divided by the difference in the two wave numbers k_e and k_o). In many crystals such as lithium niobate ($LiNbO_3$) or KDP (KH_2PO_4), the refractive indices have the property $n_e > n_o$. Some crystals such as quartz (SiO_2), $n_e < n_o$. The velocities of the two characteristic polarizations c/n_e and c/n_o are not equal. The axis along which the polarization propagates faster is called the fast axis and the other axis is called the slow axis.

Polaroid If we have a uniaxial medium given by

$$\boldsymbol{\varepsilon} = \begin{bmatrix} \varepsilon & 0 & 0 \\ 0 & \varepsilon & 0 \\ 0 & 0 & \varepsilon_z + i\dfrac{\sigma_z}{\omega} \end{bmatrix} \qquad (6.1.39)$$

we see that for an incident wave propagating in the x direction, if the electric field is polarized in the y direction, it will propagate through with a propagation constant $k_o = \omega\sqrt{\mu\varepsilon}$, which is real. However, if $\mathbf{E}$ is polarized in the z direction, it will propagate with a complex propagation constant

subscript
o
as in "o"rdinary

$$k_e = \omega\sqrt{\mu\left(\varepsilon_z + i\frac{\sigma_z}{\omega}\right)} \cong \omega\sqrt{i\mu\frac{\sigma_z}{\omega}} \quad \text{for } \frac{\sigma_z}{\omega} \gg \varepsilon_z \qquad (6.1.40)$$

and the wave will be attenuated significantly in the medium. Thus, if the thickness of the plate is large enough, an incident field with an arbitrary polarization will have its z component attenuated when passing through the plate. The transmitted field will be essentially polarized in the y direction only, which is linearly polarized.

Example An experimental setup for an absorber of laser light uses a polaroid, a quarter-wave plate, and a mirror as shown in Fig. 6.6. For an incident light with

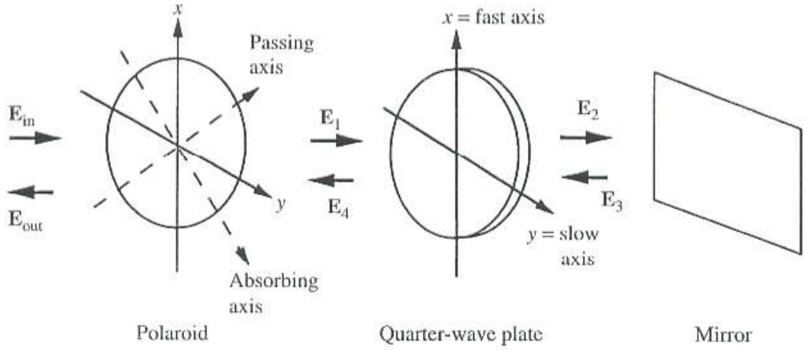

Figure 6.6 An experimental setup with a polaroid, a quarter-wave plate (QWP), and a mirror for complete absorption of the light incident from the left side.

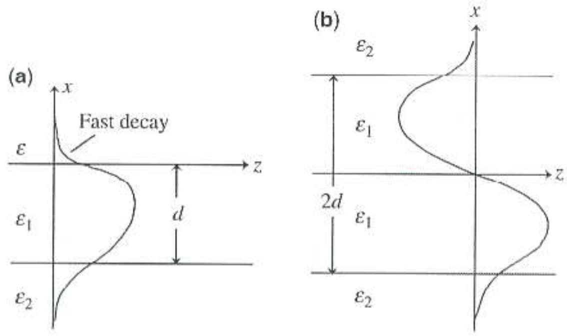

Figure 7.10 (a) An asymmetric waveguide with $\varepsilon_1 \gtrsim \varepsilon_2 \gg \varepsilon$ and a thickness d. (b) A symmetric waveguide with a thickness $2d$. The cutoff condition for the TE_m mode in (a) is equivalent to that of the $\mathrm{TE}_{(2m+1)}$ mode in (b).

which is equivalent to the cutoff condition of the $\mathrm{TE}_{(2m+1)}$ mode in a symmetric waveguide with a $2d$ thickness. This can be easily understood from a comparison of the two electric field profiles in Fig. 7.10a and Fig. 7.10b. Because the decaying constant α in region ε decays very fast in Fig. 7.10a, its field profile looks very much like half of the field profile of Fig. 7.10b.

7.2.2 TM Polarization $H = \hat{y}H_y$

field

We can easily obtain the solutions for the TM polarization using the duality principle. The ~~fled~~ has the same form as (7.2.6), except that the constant C_1 is different from that in (7.2.6) and can be derived from the normalization condition or duality principle, noting that $\varepsilon \neq \varepsilon_1 \neq \varepsilon_2$. The guidance condition is obtained from (7.2.4) after replacing μ_i by ε_i. We find

$$k_{1x}d = \tan^{-1}\left(\frac{\varepsilon_1 \alpha}{\varepsilon k_{1x}}\right) + \tan^{-1}\left(\frac{\varepsilon_1 \alpha_2}{\varepsilon_2 k_{1x}}\right) + m\pi \qquad (7.2.11)$$

for the TM_m mode.

7.3 RAY OPTICS APPROACH TO WAVEGUIDE PROBLEMS

An efficient method to find the eigenequation for the dielectric slab waveguide problem is to use the ray optics picture. We know from Section 5.3 that when a plane wave is incident on a planar dielectric boundary with an angle of incidence θ larger than the critical angle, the reflection coefficient r_{12} has a Goos–Hänchen phase shift $-2\phi_{12}$.

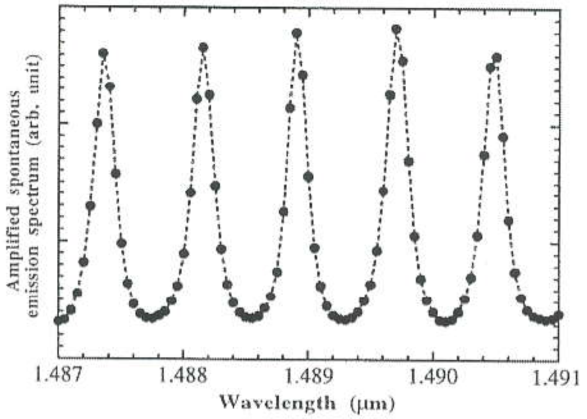

Figure 7.17 Amplified spontaneous emission spectrum of a 320-μm semiconductor laser cavity at room temperature below threshold. The injection current is $I = 8$ mA. (Above the laser threshold current, $I_{\text{th}} = 13.5$ mA, lasing starts.)

where the dispersion effect $(dn_e/d\lambda \neq 0)$ is taken into account and n_g is the group index of the guided mode, which accounts for the dispersion of the effective index $n_e(\lambda)$.

In Fig. 7.17, we show the amplified spontaneous emission spectrum of a InGaAsP/InGaAsP strained quantum-well laser at 300K. The cavity length L is 370 μm. The threshold current is $I_{\text{th}} = 13.5$ mA at this temperature. Using $n_e \simeq 3.395$ and [10, 16] $dn_e/d\lambda \simeq -0.264$ $(\mu\text{m})^{-1}$ near $\lambda = 1.49$ μm, we obtain the wavelength spacing $\Delta\lambda \simeq 7.9$ Å, which agrees with the spacing shown in the figure.

7.7 SURFACE PLASMON WAVEGUIDES

In recent years, surface plasmon waveguides, or plasmonics, has become an intensive subject of research. The main idea is to develop waveguide structures of small dimensions of subwavelength scales at optical frequencies. From Section 5.5, we understand that metals behave like plasma at optical frequencies. If the optical frequency ω is less than the plasma frequency ω_p, the permittivity

$$\varepsilon_p(\omega) = \varepsilon_0\left(1 - \omega_p^2/\omega^2\right) \tag{7.7.1}$$

becomes negative, and the wave is strongly attenuated in the metal. If $\omega > \omega_p$, the permittivity $\varepsilon(\omega)$ becomes ~~real~~ positive. At $\omega = \omega_p$, $\varepsilon(\omega) = 0$, and the propagation constant $k = \omega\sqrt{\mu\varepsilon(\omega)}$ vanishes (i.e., the electromagnetic wave does not propagate any mode). The medium response gives

$$\begin{aligned} 0 = \mathbf{D} &= \varepsilon_p(\omega)\mathbf{E} = \varepsilon_0\mathbf{E} + \mathbf{P} \\ \mathbf{P} &= -\varepsilon_0\mathbf{E}, \end{aligned} \tag{7.7.2}$$

where $U(x)$ is the Chebyshev polynomial and $x = (A + D)/2$ (see page 215). The output at the double-bus CROW structure is

$$\begin{bmatrix} c_{n+1} \\ d_{n+1} \end{bmatrix} = \frac{1}{i\kappa}\begin{bmatrix} -1 & t \\ -t & 1 \end{bmatrix}\begin{bmatrix} a_{n+1} \\ b_{n+1} \end{bmatrix}$$

$$= \frac{1}{i\kappa}\begin{bmatrix} -m_{11} + tm_{21} & -m_{12} + tm_{22} \\ -tm_{11} + m_{21} & -tm_{12} + m_{22} \end{bmatrix}\begin{bmatrix} a_1 \\ b_1 \end{bmatrix} \qquad (8.4.22)$$

where $d_{n+1} = 0$ because there is not input from the d_{n+1} port. The reflection and transmission coefficient is

$$r_{DB} = \frac{b_1}{a_1} = \frac{tm_{11} - m_{21}}{m_{22} - tm_{12}} = \frac{t[AU_{N-1}(x) - U_{N-2}(x)] - CU_{N-1}(x)}{DU_{N-1}(x) - U_{N-2}(x) - tBU_{N-1}(x)} \qquad (8.4.23)$$

$$t_{DB} = \frac{c_{n+1}}{a_1} = \frac{i\kappa}{m_{22} - tm_{12}} = \frac{i\kappa}{DU_{N-1}(x) - U_{N-2}(x) - tBU_{N-1}(x)}. \qquad (8.4.24)$$

The zeros of the reflection give the conditions for the reflection minima

$$tA - C = tU_{N-2}(x)/U_{N-1}(x). \qquad (8.4.25)$$

The poles give the oscillation conditions

$$D - tB = U_{N-2}(x)/U_{N-1}(x). \qquad (8.4.26)$$

When $N = 1$, we have

$$tA - C = 0 \qquad (8.4.27)$$

which has the solution $\theta = 2m\pi$. The ~~oscillator~~ condition is given by oscillation

$$D = tB \quad \text{or} \quad \theta = 2m\pi \quad \text{and} \quad t = 1/\sqrt{a}. \qquad (8.4.28)$$

Periodic Ring Resonators For lossless structure $a = 1$, the Bloch theorem for a periodic structure allows for

$$\begin{bmatrix} a_{n+1} \\ b_{n+1} \end{bmatrix} = e^{i\beta\Lambda}\begin{bmatrix} a_n \\ b_n \end{bmatrix} \qquad (8.4.29)$$

where $\Lambda = L_b$ is the Bragg period. We expect

$$\begin{bmatrix} A & B \\ C & D \end{bmatrix}\begin{bmatrix} a_n \\ b_n \end{bmatrix} = q\begin{bmatrix} a_n \\ b_n \end{bmatrix} \qquad (8.4.30)$$

Near $\theta = 3\pi, 7\pi, 11\pi, \ldots (4n+3)\pi$, $\sin(\theta/2) = -1$

$$\beta\Delta = 2m\pi \pm i\alpha\Lambda \tag{8.4.42}$$

$$\cosh \alpha\Lambda = -\frac{\sin(\theta/2)}{\kappa}. \tag{8.4.43}$$

A schematic plot of the dispersion relation between $\theta(=\omega n_{\text{eff}}L/c)$ versus $\beta\Lambda$ is shown in Fig. 8.21. The solid curves are the $\beta\Lambda$ or the real part of the propagation constant, and the dashed curves are for the imaginary parts $\alpha\Lambda$ in the stop bands when $\beta\Lambda = 2m\pi \pm i\alpha\Lambda$.

Figure 8.22a shows a double-ring double-bus configuration with the output as shown. Figure 8.22b shows an optical filter design for an input with two wavelengths and the drop of each wavelength at two separate horizontal straight waveguides. Figure 8.22c shows a single-bus periodic ring design for engineering the dispersion or group delay. Such a structure has been demonstrated on silicon-on-insulator (SOI) submicrometer photonic wire waveguides shown in the scanning electron microscopy (SEM) images in Fig. 8.23 [73]. The design uses coupled resonators to a curved waveguide bus for slow light or optical delay line applications. Figure 8.24a and Fig. 8.24b show the measured losses and the transmission spectra of 1 ring and 56 rings [73]. We can see a broader bandwidth when 56 rings are used. Delay of more than 10 bits at 20 Gb/s is reported using these structures.

8.5 DISTRIBUTED FEEDBACK (DFB) STRUCTURES

Consider a two-dimensional corrugated waveguide or a DFB structure [78–86] as shown in Fig. 8.25. The permittivity function $\varepsilon(x, z)$ can be written as the sum of an unperturbed slab waveguide $\varepsilon^{(0)}(x)$ and a perturbed periodic part $\Delta\varepsilon(x, z)$

$$\varepsilon(x, z) = \varepsilon^{(0)}(x) + \Delta\varepsilon(x, z). \tag{8.5.1}$$

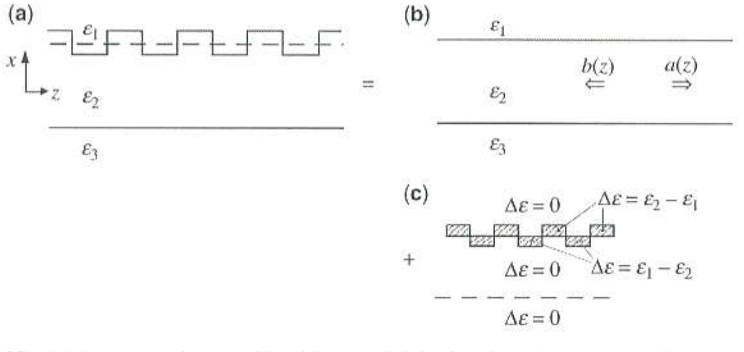

Figure 8.25 (a) A corrugated waveguide with a permittivity function $\varepsilon(x, z)$ can be written as the sum of (b) an unperturbed part $\varepsilon^{(0)}(\mathbf{r})$, which describes a uniform slab waveguide, and (c) a perturbed part $\Delta\varepsilon = \varepsilon_2 - \varepsilon_1$ or $\Delta\varepsilon = \varepsilon_1 - \varepsilon_2$ in the corrugation regions.

Because $\Delta n(z)$ is periodic, it can be decomposed into the Fourier series

$$\Delta n(z) = \sum_{p=-\infty}^{\infty} \Delta n_p \, e^{ip\frac{2\pi}{\Lambda}z}. \tag{8.5.21}$$

Therefore,

$$\begin{aligned}
&\Delta\varepsilon_p = 2n_0\,\Delta n_p \quad \text{for } |x| \le d/2, \quad \text{and} \quad \Delta\varepsilon_p = 0 \quad \text{for } |x| > d/2 \\
&K_{ab} = \frac{\omega\varepsilon_0}{4} \int\limits_{|x| \le \frac{d}{2}} \Delta\varepsilon_p(x) \left| E_y^{(0)}(x) \right|^2 dx \\
&\quad = \frac{\omega\varepsilon_0}{4}(2n_0\Delta n_{+1}) \frac{2\omega\mu}{\beta}\Gamma \\
&\quad \simeq \Gamma k_0 \Delta n_{+1}
\end{aligned} \tag{8.5.22}$$

where $k_0 = \omega\sqrt{\mu_0\varepsilon_0}$, and $\beta_0 = k_0 n_0$ have been used, and Γ is exactly the optical confinement factor because we assume the index grating is dependent on z inside the guide. Similarly,

$$K_{ba} \simeq -\Gamma k_0 \Delta n_{-1} \tag{8.5.23}$$

and we have kept $p = +1$ or -1 for the first-order grating.

For an index phase grating with a magnitude Δn and phase φ,

$$\begin{aligned}
\Delta n(z) &= \Delta n \cos\left(\frac{2\pi}{\Lambda}z + \varphi\right) \\
&= \Delta n_{+1}\, e^{i\frac{2\pi}{\Lambda}z} + \Delta n_{-1}\, e^{-i\frac{2\pi}{\Lambda}z} \\
\Delta n_{+1} &= \frac{\Delta n}{2}\, e^{i\varphi}, \qquad \Delta n_{-1} = \frac{\Delta n}{2}\, e^{-i\varphi}.
\end{aligned} \tag{8.5.24}$$

The coupling coefficients are

$$K_{ab} = \Gamma k_0 \frac{\Delta n}{2}\, e^{i\varphi} \tag{8.5.25a}$$

$$K_{ba} = -\Gamma k_0 \frac{\Delta n}{2}\, e^{-i\varphi} = -K_{ab}^{*}$$

(8.5.25~~a~~) ← b

In other words, the coupling coefficients can be put in very simple forms and they satisfy the relation $K_{ba} = -K_{ab}^{*}$ because the index grating is lossless.

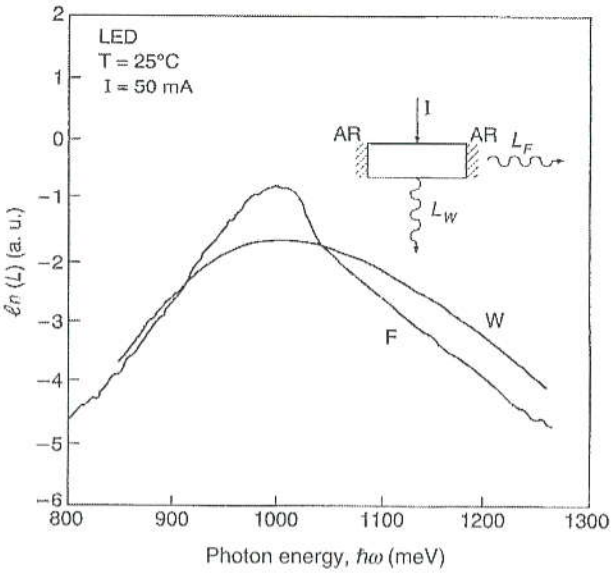

Figure 10.8 Measured spontaneous emission spectrum obtained by collecting photons through a window (W) in the substrate L_W and the amplified spontaneous emission spectrum obtained by collecting photons from the facet (F) L_F of an LED. (Reprinted with permission from [42] © 1993 American Institute of Physics.)

where $G_n(\hbar\omega) = \Gamma g - \alpha_i$ is the net modal gain (including all the losses due to absorptions and scatterings in the device). Note that at the transparency wavelength, $G_n(\hbar\omega) = 0$ and $L_F(\hbar\omega) = L_W(\hbar\omega)$ when no amplification by the gain action exists. With enough carrier injection such that $G_n > 0$, we see that the photon density in the spectral region where $g(\hbar\omega)$ is positive will experience amplification whereas that outside the positive gain region will experience absorption. Because the gain spectrum is narrower than that of the spontaneous emission spectrum [46], the facet light will be narrower than that of the window light. These results [42] are shown in Fig. 10.8. As a matter of fact, a comparison of these two spectra has been used to extract the gain spectrum of a laser diode structure. By measuring the two spectra $L_F(\hbar\omega)$ and $L_W(\hbar\omega)$ at the same current injection level, we can obtain the gain spectrum. Furthermore, if we take the logarithmic function of the ratio of the two spectra, ln $[L_F(\hbar\omega)/L_W(\hbar\omega)]$, it will be close to that of the gain spectrum because it is proportional to $\ln[(e^{G_nL} - 1)/G_n] \sim (\Gamma g_{\cancel{n}} - \alpha_i)L$ if the overall gain ($G_nL \gg 1$) is large enough [43]. By fitting the gain spectrum with a theoretical gain model, we can extract the carrier density n at a given injection current I [43]. The carrier density versus the injection current I is a monotonically increasing function of I, as shown in Fig. 10.9a at 25°C and Fig. 10.9b at 55°C. For laser diodes, the carrier density is pinned at the threshold value when the injection current is increased beyond threshold.

delete
subscript n

current density is called the transparent current density. Further increase of the current increases gain until it reaches the threshold condition, at which the gain is equal to the background absorption plus the mirror transmission loss (or laser output) of the cavity.

Consider an optical field $E_{\mathrm{sp}}(\lambda)$ due to the spontaneous emission of photons by electron–hole radiative recombinations in a Fabry–Perot cavity. When the optical field propagates toward the minor facets with optical field reflection coefficients r_1 and r_2 on each facet, we can write down the multiple reflections of the optical field as

$$E_{\mathrm{ASE}}(\lambda) = E_{\mathrm{sp}}(\lambda)\left[1 + r_1 r_2 e^{i2kL} + \left(r_1 r_2 e^{i2kL}\right)^2 + \cdots\right] = \frac{E_{\mathrm{sp}}(\lambda)}{1 - r_1 r_2 e^{i2kL}}. \tag{10.1.29}$$

The complex propagation constant has a real and imaginary part

$$k = k' - i\frac{G_n}{2} = \frac{2\pi}{\lambda} n_{\mathrm{e}} - i\frac{G_n}{2} \tag{10.1.30a}$$

$$G_n = \Gamma g - \alpha_{\mathrm{i}} = \text{The } \textit{net} \text{ modal gain.} \tag{10.1.30b}$$

The measured ASE power spectrum is proportional to $|E_{\mathrm{ASE}}(\lambda)|^2$

$$I(\lambda) = |E_{\mathrm{ASE}}(\lambda)|^2 = \frac{|E_{\mathrm{sp}}(\lambda)|^2}{|1 - r_1 r_2 e^{i2kL}|^2} = \frac{|E_{\mathrm{sp}}(\lambda)|^2}{(1-A)^2 + 4A\sin^2(k'L)} \tag{10.1.31}$$

where the amplitude A is

$$A = \sqrt{R_1 R_2}\, e^{G_n L}, \quad R_1 = |r_1|^2, \quad R_2 = |r_2|^2. \tag{10.1.32}$$

The ASE spectrum has maxima at

$$k'L = m\pi, \quad I_{\max} = \frac{|E_{\mathrm{sp}}(\lambda_{\max})|^2}{(1-A)^2} \tag{10.1.33a}$$

and minima at

$$k'L = \left(m + \frac{1}{2}\right)\pi, \quad \underbrace{I_{\min}\cancel{(\lambda)} = \frac{|E_{\mathrm{sp}}(\lambda_{\min})|^2}{(1+A)^2}.}_{\longrightarrow\ I_{\min}} \tag{10.1.33b}$$

If we take the ratio between two *nearby* peak and valley of the ASE spectrum,

$$\frac{I_{\max}}{I_{\min}} = \frac{(1+A)^2}{(1-A)^2} \tag{10.1.34a}$$

Because $k_z/\omega\mu$ is a constant for a given mode, we can simply use

$$\Gamma = \frac{\int\int_{\text{active}} |E_y(x, y)|^2 dxdy}{\int_{-\infty}^{\infty}\int_{-\infty}^{\infty} |E_y(x, y)|^2 dxdy} \simeq \Gamma_x \Gamma_y \tag{10.2.11}$$

which is approximated by the product of the two optical confinement factors along the x direction (with a slab geometry in the effective index method) and along the y direction when the field is approximately given by

$$E_y \simeq F(x)\, G(y). \tag{10.2.12}$$

It is a good approximation for a strongly index-guided structure, and $F(x, y) \simeq F(x)$ if the geometry along the y direction is uniform such that the first part of the wave function $F(x, y)$ in the effective index method described in Section 7.5 can be assumed to be independent of y. Index-guided semiconductor lasers have been shown to exhibit excellent performance including the fundamental mode operation, low threshold, high quantum efficiency, and low temperature sensitivity [33].

10.3 QUANTUM-WELL LASERS

Quantum-well (QW) structures [12–16, 61], as shown in Fig. 10.19, have been used as the active layer of semiconductor laser diodes with reduced threshold current densities compared with those for conventional double-heterostructure (DH) semiconductor diode lasers. Research on quantum-well physics and semiconductor lasers has been of great interest recently. For a brief history, see Ref. 3. Various designs such as single quantum well (SQW), multiple quantum well (MQW), and graded-index separate-confinement heterostructures (GRINSCH) have been used for semiconductor lasers [21]. As we have seen in Chapter 9, quantum-well structures show quantized subbands and step-like densities of states. The density of states for a quasi-two-dimensional structure has been used to reduce threshold current density and improve temperature stability. Energy quantization provides another degree of freedom to tune the lasing wavelength by varying the well width and the barrier height. Scaling laws for quantum-well lasers and quantum-wire lasers show significant reduction of threshold current in reduced dimensions [24].

10.3.1 A Simplified Gain Model

The simplest model we will consider is the gain spectrum based on (9.4.~~18~~13) for a finite temperature, assuming a zero scattering linewidth [62, 63]

$$g(h\omega) = \sum_{n,m} g_{\max}[f_c^n(E_t = \hbar\omega - E_{hm}^{en}) - f_v^m(E_t = \hbar\omega - E_{hm}^{en})]H(\hbar\omega - E_{hm}^{cn}) \tag{10.3.1a}$$

where

$$g_{\max} = C_0|\hat{e}\cdot\mathbf{M}|^2 |I_{hm}^{en}|^2 \rho_r^{2D} \simeq C_0|\hat{e}\cdot\mathbf{M}|^2 \rho_r^{2D}\delta_{nm} \tag{10.3.1b}$$

$$C_0 = \frac{\pi e^2}{n_r c \varepsilon_0 m_0^2 \omega} \qquad \rho_r^{2D} = \frac{m_r^*}{\pi\hbar^2 L_z} \tag{10.3.1c}$$

(a) Single-Quantum-Well Separate-Confinement Heterostructure

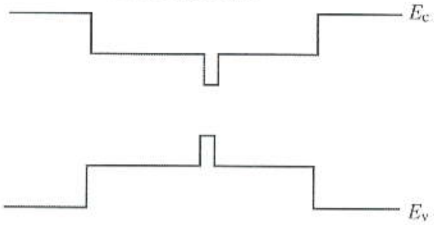

(b) Multiple-Quantum-Well Separate-Confinement Heterostructure

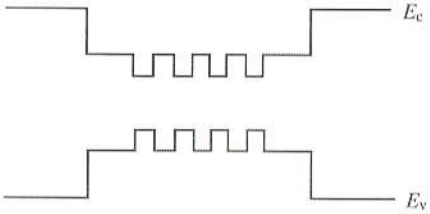

(c) Graded-Index Separate-Confinement Heterostructure (GRINSCH)

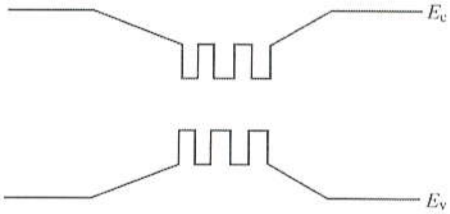

Figure 10.19 Band-gap profiles for (a) single-quantum-well, (b) multiple-quantum-well, and (c) graded-index separate-confinement heterostructure (GRINSCH) semiconductor lasers.

ρ_r^{2D} (Insert)

is the reduced joint density of states. The overlap integral between the *n*th conduction subband and the *m*th hole subband is usually very close to unity for $n = m$, and it vanishes if $n \neq m$ because of the even–odd parity consideration. The polarization-dependent momentum matrix element is listed in Table 9.1 for conduction to heavy-hole and light-hole band transitions. The occupation factors for the electrons in the *n*th conduction subband and the electrons in the *m*th hole subband are

$$f_c^n(E_t = \hbar\omega - E_{hm}^{en}) = \frac{1}{1 + e^{\left[E_{en} + (m_r^*/m_c^*)(\hbar\omega - E_{hm}^{en}) - F_c\right]/k_B T}} \tag{10.3.2a}$$

$$f_v^m\left(E_t = \hbar\omega - E_{hm}^{en}\right) = \frac{1}{1 + e^{\left[E_{hm} - (m_r^*/m_h^*)(\hbar\omega - E_{hm}^{en}) - F_v\right]/k_B T}}. \tag{10.3.2b}$$

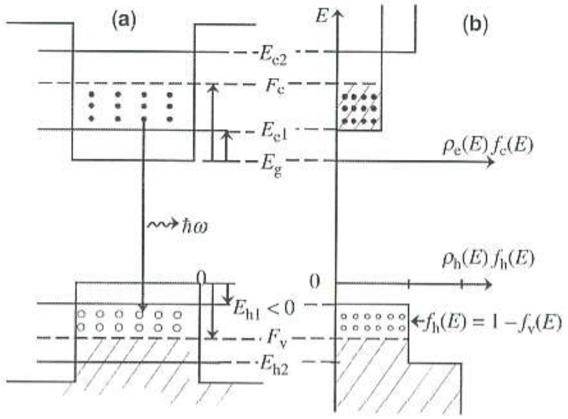

Figure 10.20 (a) Population inversion in a quantum-well structure, where $E_g + F_c - F_v > \hbar\omega > E_{e1} - E_{h1} + E_g$. (b) The product of the conduction band density of states $\rho_e(E)$ and the Fermi–Dirac occupation probability $f_c(E)$ for the calculation of the electron density n is plotted versus the energy E in the vertical scale. Similarly, $\rho_h(E) f_h(E) = \rho_h(E)\,[1 - f_v(E)]$ is plotted versus E for the energy ($E < 0$) in the valence band. Assume that the temperature T is 0K.

Gain occurs when $f_c^n > f_v^m$, that is, the population inversion is achieved, Fig. 10.20. It also leads to $E_g + F_c - F_v > \hbar\omega$, where F_c and F_v are the quasi-Fermi levels for electrons and holes, measured from the conduction and valence band edges, respectively. Only those electrons and holes satisfying the k-selection rule contribute significantly to the gain process.

10.3.2 Determination of Electron and Hole quasi-Fermi Levels

The quasi-Fermi levels F_c and F_v are determined by the carrier concentrations n and p, which satisfy the charge neutrality condition

$$n + N_A^- = p + N_D^+ \tag{10.3.3}$$

$$n = \int_0^{\infty} dE\, \rho_e(E) f_c(E), \quad p = \int_{-\infty}^{\infty} dE\, \rho_h(E)[1 - f_v(E)]$$

$$\rho_e(E) = \frac{m_e^*}{\pi\hbar^2 L_z} \sum_{n=1}^{\infty} H(E - E_{en}) \tag{10.3.4}$$

subscript z

$$\rho_h(E) = \frac{m_h^*}{\pi\hbar^2 LZ} \sum_{m=1}^{\infty} H(E_{hm} - E)$$

where $H(x)$ is the Heaviside step function, $H(x) = 1$ if $x > 0$, and $H(x) = 0$ if $x < 0$. In Fig. 10.21a and Fig. 10.21b, we plot the products $\rho_e(E) f_c(E)$ and $\rho_h(E)\,[1 - f_v(E)]$ versus the energy E for $T = 0$K and 300K, respectively. The areas below these functions give the carrier concentrations n and p.

Figure 10.43 shows [133] an example of self-organized InAs quantum dots inserted in InGaAs quantum well grown on a GaAs substrate by molecular-beam epitaxy. Room temperature photoluminescence spectrum shows that QD emission wavelength is controllable from 1.1 to 1.3 μm by varying the composition of $In_xGa_{1-x}As$ quantum-well matrix from $x = 0$ (1.1 μm for GaAs matrix) to $x = 0.3$ (1.3 μm). Figure 10.44a [133] shows the plan-view bright-field TEM image along [100] direction and Fig. 11.44b the cross-section image under dark-field (200) condition for the InAs QD array in a 10-nm $In_{0.12}Ga_{0.88}As$ quantum well. InAs-rich clusters in the region of smaller InAs content are seen in both observation views. The surface density of the islands is estimated as $(3-4) \times 10^{10}$ cm^{-2}. The dots have a typical lateral size of about 20 nm and a height of 5–6 nm. These sizes are larger than those of the InAs islands formed in a GaAs matrix. Because both the QD and QW materials are lattice mismatched to the GaAs substrate, there is a risk of plastic strain relaxation. Nevertheless, no misfit dislocations are revealed by TEM due to the choice of the QW width and the InAs ~~model~~ mole fraction in the QW [133]. The sample with the QD structure embedded in a vertical optical microcavity shows a Photoluminescence (PL) emission of 1.33 μm [133].

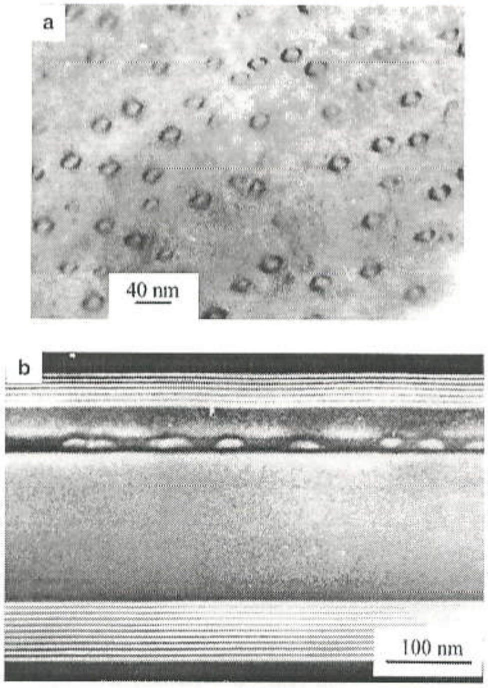

Figure 10.44 (a) Plan-view of the bright-field TEM image along the [100] zone, and (b) the image of the cross section under dark-field (200) condition for the structure containing InAs QD array in a 10-nm $In_{0.12}Ga_{0.88}As$ QW. (Reprinted with permission from [133] © 1999 American Institute of Physics.)

10.5.2 Spontaneous Emission, Gain, and Lasing Spectrum

In Chapter 9, we discussed the absorption and gain of quantum-dot lasers [140–146]. The filling of states of quantum dots is complicated by the inhomogeneous size distribution and the density of dots or the distance between nearby dots [141]. When the inhomogeneous broadening is reduced, clear observation of ground-state and excited-state emission peaks or absorption peaks are observable [141–146]. For example, Fig. 10.45a [141] shows the net ~~model~~ modal absorption of a quantum-dot sample (dots in a well, or DWELL [139]) showing clear absorption peaks at the ground state and excited state when there is no current injection. In the presence of increasing current, population inversion occurs and a clear gain peak occurs at the ground state or the excited state at a higher current of 200 mA. Analysis of the gain spectrum seems to indicate two quasi-Fermi levels for the ground and excited state. The competition of homogenous broadening and inhomogeneous broadening also leads to

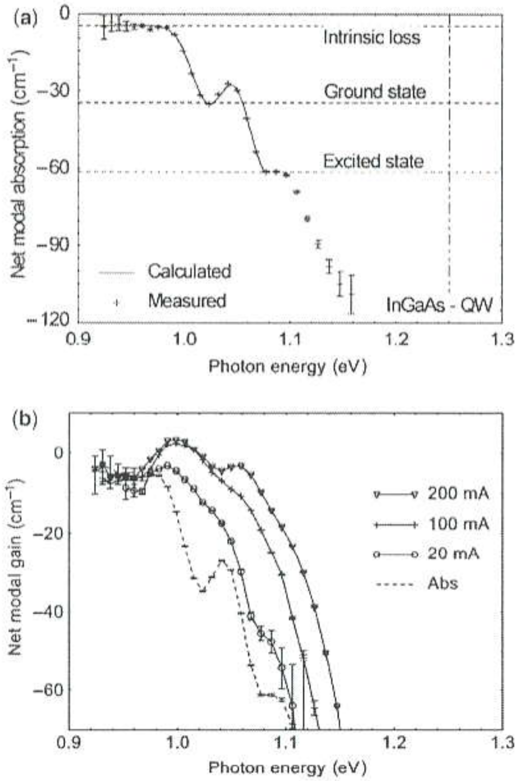

Figure 10.45 (a) The net modal absorption of the three-layer dots-in-well (DWELL) waveguide structure for TE-polarized light. The vertical line indicates the transition energy of the well. The horizontal dashed lines indicate the waveguide loss and the peak absorptions due to the ground and excited states. The solid line is the fitting of the calculated absorption spectrum to the experimental data. (b) The net modal TE gain spectra for pulsed currents per segment from 20 to 200 mA. (Reprinted with permission from [141] © 2004 IEEE.)

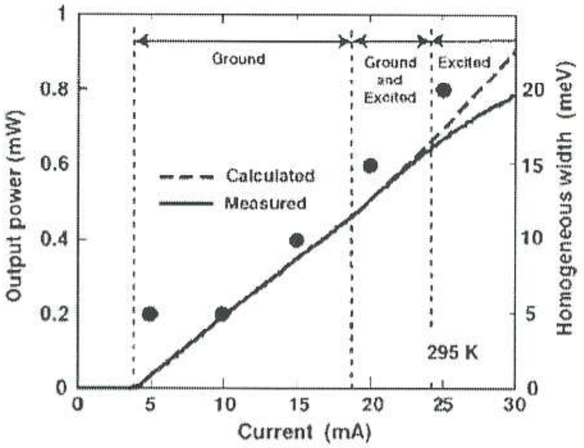

Figure 10.47 Output power and the homogeneous broadening of the ground-state transition (solid circles) versus the injection current at 295K. The solid curve is the measurement, and the dashed curve is the calculation. The range of current for only the ground-state lasing, both the ground-state and excited-state lasings, and only the excited-state lasing is shown, with the perpendicular dashed lines as boundaries. (Reprinted with permission from [142] © 2005 American Institute of Physics.)

only the excited state are marked. The homogenous linewidth, which is used to model the lasing spectrum, is also shown as the right vertical axis.

10.5.3 High-Speed Modulation: *p*-Doping and Tunneling Injection

***p*-Type Doping [147–162]** A few major improvements in quantum-dot lasers result from the *p*-type doping, tunneling injection, and submonolayer growth (for a recent review, see [137]. *p*-type doping was suggested as early as 1988 [127] to improve the gain property of quantum-dot lasers. A simple way to understand the advantage of *p*-type doing is that the heavy-hole subband energy levels are close to each other due to their heavier effective mass than that of the electrons in the conduction band. Therefore, the holes spread out thermally into various subbands instead of filling the ground state completely first, whereas electrons tend to occupy the ground state better because the excited state of the conduction subband (C2) is further away from the ground state (C1). It implies that the number of interband transitions such as C1-HH1 is reduced because not all holes occupy the ground state (HH1) for an undoped quantum dot sample. The holes that spread out to HH2 subband do not recombine effectively with those electrons of the C1 subband. Although this is an oversimplified picture, theoretical models and experimental data seem to confirm several advantages of *p*-type doping. Experimental results have indeed shown that the *p*-doped 1.3-μm QD lasers have substantially improved performance for short cavity lengths, indicating an increase in the ground state gain and exhibit excellent temperature sensitivity [147–149]. Further experimental data [149] on spontaneous and laser emission of *p*-doped and undoped QD heterostructures indeed show that the ground-state spontaneous emission of the carbon-doped

insensitivity

12.2 HIGH-SPEED MODULATION RESPONSE WITH NONLINEAR GAIN SATURATION

12.2.1 Nonlinear Gain Saturation

The nonlinear gain model $g(n, S)$ at high photon density S can be taken from [12, 13]

$$g(n, S) = \frac{g(n_0) + g'(n(t) - n_0)}{1 + \varepsilon S(t)} \qquad (12.2.1)$$

where $g_0 = g(n_0)$ and $g' = [\partial g/\partial n]_{n=n_0}$ is the differential gain at n_0. The factor $1 + \varepsilon S$ accounts for nonlinear gain saturation, which is important when the photon density is large. The factor ε is called the gain suppression coefficient.

dc Solution The steady-state solution at $I = I_0$ is obtained from $d/dt = 0$ in the rate equations

$$\eta_i \frac{J_0}{qd} = \frac{n_0}{\tau} + \frac{v_g g_0 S_0}{1 + \varepsilon S_0} \qquad (12.2.2)$$

$$\Gamma \frac{v_g g_0 S_0}{1 + \varepsilon S_0} = \frac{S_0}{\tau_p} - \beta R_{sp}(n_0). \qquad (12.2.3)$$

If $\varepsilon \neq 0$, the general solution for S_0 can be found analytically from (12.2.3) (see Problem 12.5). Then n_0 is obtained from (12.2.2).

Small Signal ac Analysis Using the linearized expression by substituting (12.1.10) into (12.2.1), we obtain

$$g(n, S) = \frac{g(n_0)}{1 + \varepsilon S_0} + \frac{g'}{1 + \varepsilon S_0} \Delta n(t) - \frac{g_0}{(1 + \varepsilon S_0)^2} \varepsilon s(t). \qquad (12.2.4)$$

The small signal ac responses $\Delta n(t)$ and $s(t)$ satisfy the following equations

t

$$\frac{d}{dt}\begin{bmatrix} \Delta n(t) \\ s(t) \end{bmatrix} + \begin{bmatrix} A & D \\ -C & B \end{bmatrix}\begin{bmatrix} \Delta n(t) \\ s(t) \end{bmatrix} = \begin{bmatrix} \eta_i j(\omega)/qd \\ 0 \end{bmatrix} \qquad (12.2.5)$$

where A, B, C, and D are defined as

$$A = \frac{1}{\tau} + \frac{v_g g' S_0}{1 + \varepsilon S_0} \qquad B = \frac{1}{\tau_p} - \frac{\Gamma v_g g_0}{(1 + \varepsilon S_0)^2}$$

$$C = \frac{\Gamma v_g g' S_0}{1 + \varepsilon S_0} \qquad D = \frac{v_g g_0}{(1 + \varepsilon S_0)^2}. \qquad (12.2.6)$$

small-signal frequency response of the test laser for optical modulation from the pump laser and use the same rate equations with a different source term to derive the electrical modulation response of the test laser.

Electrical Injection For electrical microwave modulation, the electrons are injected from the outer edge of the left separate-confinement-heterostructure (SCH) region and the holes from the outer edge of the right SCH region. The injected carriers diffuse through the SCH region and are captured into the QWs before recombining via the stimulated emission process. The transport effects can be modeled by taking into account the carrier density in the SCH region, the carrier density in the well region, and the photon density separately. Coupling of the carrier density in the barrier states above the QWs to the carrier density in the QWs is modeled by two terms representing carrier capture and escape into or from the wells, respectively. In this case, three rate equations are needed. The source term enters through the injection current in electrical modulation. The model considers carrier injection from the outer edges of the SCH region, diffusion across the SCH region, and the subsequent capture and emission of carriers by the QW.

Optical Injection For optical injection using an external pump laser, the pump photon density acts as the source term. Because the optical energy of the pump laser determines whether the photons are absorbed in the well or in the barriers, we choose the pump wavelength to be longer than the band-gap wavelength of the barriers and shorter than the band-edge wavelength of the wells so that absorption occurs only in the wells. Compared with electrical modulation, optical modulation with an optical energy in the absorption range of the QW directly produces photon-generated carriers inside the test laser's active region via the injection of a modulated laser beam through one of the test laser's mirror facets. Therefore, the majority of carriers transporting through the SCH region is not required for lasing action, although the coupling between SCH and QW states still exists for optical modulation. In this way, optical modulation removes the severe low-frequency roll-off due to the transport and parasitic effects and helps to clarify the intrinsic response.

The rate equations for both electrical and optical injections are written as

$$\frac{dN_b(t)}{dt} = \eta_i \frac{I(t)}{qV_b} - \frac{N_b(t)}{\tau_b} - \frac{N_b(t)}{\tau_{bw}} + \frac{N_w(t)V_w}{\tau_{wb}V_b} \tag{12.3.1}$$

$$\frac{dN_w(t)}{dt} = \frac{N_b(t)V_b}{\tau_{bw}V_w} - \frac{N_w(t)}{\tau_w} - \frac{N_w(t)}{\tau_{wb}} - \mathrm{v}_g \frac{g(N_w)}{1+\varepsilon S(t)} S(t) + \mathrm{v}_g \alpha_p S_p(t) \tag{12.3.2}$$

$$\frac{dS(t)}{dt} = \Gamma \mathrm{v}_g \frac{g(N_w)}{1+\varepsilon S(t)} S(t) - \frac{S(t)}{\tau_p} \tag{12.3.3}$$

S(t)
$S_p(t)$
S(t)
S(t)
S(t)

where q is the electron unit charge, $g(N_w)$ is the optical gain at the carrier concentration N_w in the bound states of the wells, N_b is the carrier density in the barrier (continuum) states including the SCH and active layers, S is the photon density of

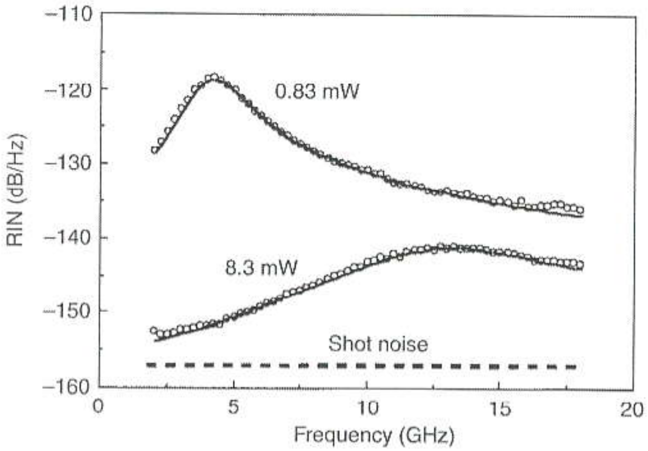

Figure 12.12 The relative intensity noise (RIN) spectrum as two bias currents above threshold. The symbols are experimental data and the solid curves are the theoretical fits. The shot noise background is also shown as the dashed line. (Reprinted with permission from [86] © 1992 IEEE.)

of the frequency. The RIN spectrum is thus given by

$$\frac{\mathrm{RIN}}{\Delta f} = \frac{2S_{\delta p}(\omega)}{P_0^2}. \tag{12.5.12}$$

Further derivations for the spectral density using (12.5.6) and (12.5.7) lead to [83, 85]

$$S_{\delta p}(\omega) = \hbar\omega P_0\left[(a_1 + a_2\omega^2)\frac{|H(\omega)|^2}{\omega_r^4} + 1\right] \tag{12.5.13}$$

$$\frac{\mathrm{RIN}}{\Delta f} = \frac{2\hbar\omega}{P_0}\left[(a_1 + a_2\omega^2)\frac{|H(\omega)|^2}{\omega_r^4} + 1\right]. \tag{12.5.14}$$

Typically, the last term (one) in the square bracket of (12.5.14) is much smaller than the leading two terms, and is thus negligible [85]. The expression requires essentially four parameters: a_1, a_2, ω_r, and γ, which can be extracted by fitting the experimental RIN spectrum at various bias current above threshold. Figure 12.12 shows an example of the RIN spectrum at two bias currents (symbols: experimental data; solid curves: theory) [86]. The extracted relaxation frequency from the peak of the RIN spectrum shows a linear dependence on the square root of the optical power output. The damping factor γ also shows a linear dependence on the squared ~~relation~~ relaxation frequency with the slope determined by the K factor. The RIN characteristics of a semiconductor laser under the injection locking condition shows a reduction in the RIN noise floor as well as an increase of the relaxation frequency controllable by the injection laser power and detuning [87].

13.3.2 Directional Coupler Modulator

For an incident optical beam into waveguide a in a directional coupler modulator, the output power is

$$P_b = |b(\ell)|^2 = \frac{|K|^2}{\Psi^2}\sin^2(\Psi\ell) \tag{13.3.7a}$$

$$\Psi = \left[\left(\frac{\Delta\beta}{2}\right)^2 + K^2\right]^{1/2} \tag{13.3.7b}$$

and

$$P_a = P_{\text{in}} - P_b = 1 - |b(\ell)|^2 \tag{13.3.8}$$

where the input power is assumed to be 1. Because $\Delta\beta \simeq \beta_a - \beta_b = kn_o^3 r_{63} V/d$, we plot the output power P_a versus $\Delta\beta\ell$. Suppose we design the modulator with a length ℓ such that $P_a = 0$, and $P_b = 1$, at $\Delta\beta = 0$ (i.e., $K\ell = \pi/2$). In order to switch to $P_a = 1$, and $P_b = 0$, we require at least $\Delta\beta\ell = \sqrt{3}\pi$, assuming the field-induced change in the refractive index affects the coupling coefficient negligibly. (Otherwise, we can calculate the field-dependent K and still use the expressions for P_a and P_b in (13.3.7) and (13.3.8) to find the output powers.) To switch from a cross state to a parallel state, the applied voltage has to be large enough such that $\Delta\beta\ell = \sqrt{3}\pi$ is satisfied. A plot of P_a versus $\Delta\beta\ell$ for $K\ell = \pi/2$ is shown as the thick solid curve in Fig. 13.10. We also plot P_a versus $\Delta\beta\ell$ for $K\ell = \pi$, and $K\ell = 3\pi/2$. We see that complete switching from the ⊗ (cross) state to the ⊖ (parallel) state is possible (for $K\ell = \pi/2$ or $3\pi/2$). For $K\ell = \pi$, where we start with the parallel state at $\Delta\beta\ell = 0$, it is impossible to switch to the ⊗ state simply by changing $\Delta\beta\ell$ alone. This fact can also be checked with the switching diagram in Fig. 8.11.

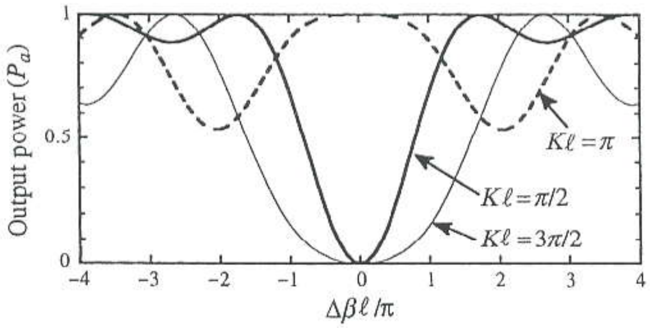

Figure 13.10 The output power from waveguide a as a function of $\Delta\beta L$ for $K\ell = \pi/2$, π, and $3\pi/2$ for a directional coupler modulator.

ℓ

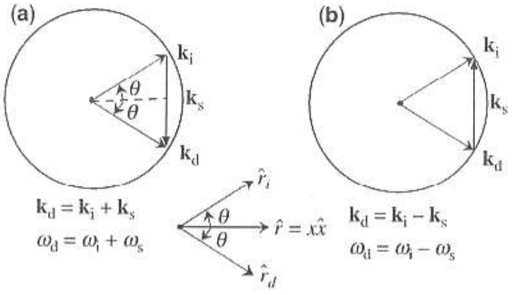

Figure 13.14 The diagrams for the diffraction of light by sound: (a) $\mathbf{k}_{\rm d} = \mathbf{k}_{\rm i} + \mathbf{k}_{\rm s}$, $\omega_{\rm d} = \omega_{\rm i} + \omega_{\rm s}$, and (b) $\mathbf{k}_{\rm d} = \mathbf{k}_{\rm i} - \mathbf{k}_{\rm s}$, $\omega_{\rm d} = \omega_{\rm i} - \omega_{\rm s}$.

reduced

Similarly, (13.5.13) corresponds to the emission of a phonon from the incident photon. Here h is the Planck constant. Also noting that $k_{\rm i} - \frac{\omega_{\rm i}}{c} n$, and $k_{\rm d} = \frac{\omega_{\rm d}}{c} n$, we find from (13.5.6) and (13.5.10)

$$i\mathbf{k}_{\rm i} \cdot \nabla E_{\rm i} = ik_{\rm i} \frac{\partial E_{\rm i}}{\partial r_{\rm i}} = -\frac{\omega_{\rm i}^2 n}{2c^2} \Delta n E_{\rm d}(r).$$

Because $\mathbf{r}_{\rm i}$ is along the direction of $\mathbf{k}_{\rm i}$, and $\mathbf{r}_{\rm d}$ is along the direction of $\mathbf{k}_{\rm d}$, we take $\mathbf{r}$ along the x direction, and

$$r_{\rm i} \cos\theta = x, \qquad r_{\rm d} \cos\theta = x. \tag{13.5.14}$$

We obtain

$$\frac{dE_{\rm i}}{dx} = iK_{\rm id} E_{\rm d} \qquad K_{\rm id} = \frac{\omega_{\rm i} \Delta n}{2c\cos\theta} \tag{13.5.15a}$$

$$\frac{dE_{\rm d}}{dx} = iK_{\rm di} E_{\rm i} \qquad K_{\rm di} = \frac{\omega_{\rm d} \Delta n}{2c\cos\theta}. \tag{13.5.15b}$$

Because $\omega_{\rm s} \ll \omega_{\rm i}$, $\omega_{\rm d}$ we have $\omega_{\rm d} \sim \omega_{\rm i} \equiv \omega$ and $K_{\rm di} \simeq K_{\rm id} \equiv K$

$$K = \frac{\omega \Delta n}{2c\cos\theta}. \tag{13.5.16}$$

The solutions for the coupled-mode equation given the initial conditions $E_{\rm i}(0)$ and $E_{\rm d}(0)$ are

$$\begin{aligned} E_{\rm i}(x) &= E_{\rm i}(0)\cos Kx + iE_{\rm d}(0)\sin Kx \\ E_{\rm d}(x) &= E_{\rm d}(0)\cos Kx + iE_{\rm i}(0)\sin Kx. \end{aligned} \tag{13.5.17}$$

If initially, $E_{\rm d}(0) = 0$, the field amplitudes are

$$E_{\rm i}(x) = E_{\rm i}(0)\cos Kx \qquad E_{\rm d}(x) = iE_{\rm i}(0)\sin Kx. \tag{13.5.18}$$

4. S. Adachi, *Physical Properties of III–V Semiconductor Compounds*, Wiley, New York, 1992.
5. K. H. Hellwege, Ed., *Landolt–Börnstein Numerical Data and Functional Relationships in Science and Technology*, New Series, Group III **17a**, Springer-Verlag, Berlin, 1982; Groups III–V **22a**, Springer-Verlag, Berlin, 1986.
6. K. Tada and N. Suzuki, "Linear electrooptical properties of InP," *Jpn. J. Appl. Phys.* **19**, 2295–2296 (1980); and N. Suzuki and K. Tada, "Electrooptic properties and Raman scattering in InP," *Jpn. J. Appl. Phys.* **23**, 291–295 (1984).
7. S. Adachi and K. Oe, "Linear electro-optic effects in zincblende-type semiconductors: key properties of InGaAsP relevant to device design," *J. Appl. Phys.* **56**, 74–80 (1984); and "Quadratic electrooptic (Kerr) effects in zincblende-type semiconductors: Key properties of InGaAsP relevant to device design," *J. Appl. Phys.* **56**, 1499–1504 (1984).
8. S. Adachi, *Properties of Indium Phosphide*, INSPEC, The Institute of Electrical Engineers, London and New York, 1991.
9. A. K. Ghatak and K. Thyagarajan, *Optical Electronics*, Cambridge University Press, Cambridge, UK, 1989.
10. M. Abramowitz and I. A. Stegun, Eds., *Handbook of Mathematical Functions with Formulas, Graphs, and Mathematical Tables*, Chapter 9, Dover, New York, 1972.
11. S. Thaniyavarn, "Optical modulation: electrooptical Devices," Chapter 4 in K. Chang, Ed., *Handbook of Microwave and Optical Components*, vol. 4 of *Fiber and Electro-Optical Components*, Wiley, New York, 1991.
12. H. Nishihara, M. Haruna, and T. Suhara, *Optical Integrated Circuits*, McGraw-Hill, New York, 1989.
13. T. Tamir, Ed., *Guided-Wave Optoelectronics*, 2nd ed., Springer-Verlag, Berlin, 1990.
14. R. C. Alferness, "Guided-wave devices for optical communication," *IEEE J. Quantum Electron.* **QE-17**, 946–959 (1981).
15. O. G. Ramer, "Integrated optic electrooptic modulator electrode analysis," *IEEE J. Quantum Electron.* **QE-18**, 386–392 (1982).
16. D. Marcuse, "Optimal electrode design for integrated optics modulators," *IEEE J. Quantum Electron.* **QE-18**, 393–398 (1982).
17. H. Kogelnik and R. V. Schmidt, "Switched directional couplers with alternating $\Delta\beta$," *IEEE J. Quantum Electron.* **QE-12**, 396–401 (1976).
18. K. Noguchi, O. Mitomi, H. Miyazawa, and S. Seki, "A broadband Ti:LiNbO$_3$ optical modulator with a ridge structure," *J. Lightwave Technol.* **13**, 1164–1168 (1995).
19. O. Mitomi, K. Noguchi, and H. Miyazawa, "Design of ultra-broadband LiNbO$_3$ optical modulators with ridge structure," *IEEE Trans. Microwave The. Techn.* ~~41~~, 2203–2207 (1995). 43 (Bold)
20. O. Mitomi, K. Noguchi, and H. Miyazawa, "Broadband and low driving-voltage LiNbO$_3$ optical modulators," *IEE Proc. Optoelectron.* **145**, 360–364 (1998).
21. E. L. Wooten, K. M. Kissa, A. Yi-Yan, E. J. Murphy, D. A. Lafaw, P. F. Hallemeier, D. Maack, D. V. Attanasio, D. J. Fritz, G. J. McBrien, and D. E. Bossi, "A review of lithium niobate modulators for fiber-opticcommunications systems," *IEEE J. Sel. Top. Quantum Electron.* **6**, 69–82 (2000).

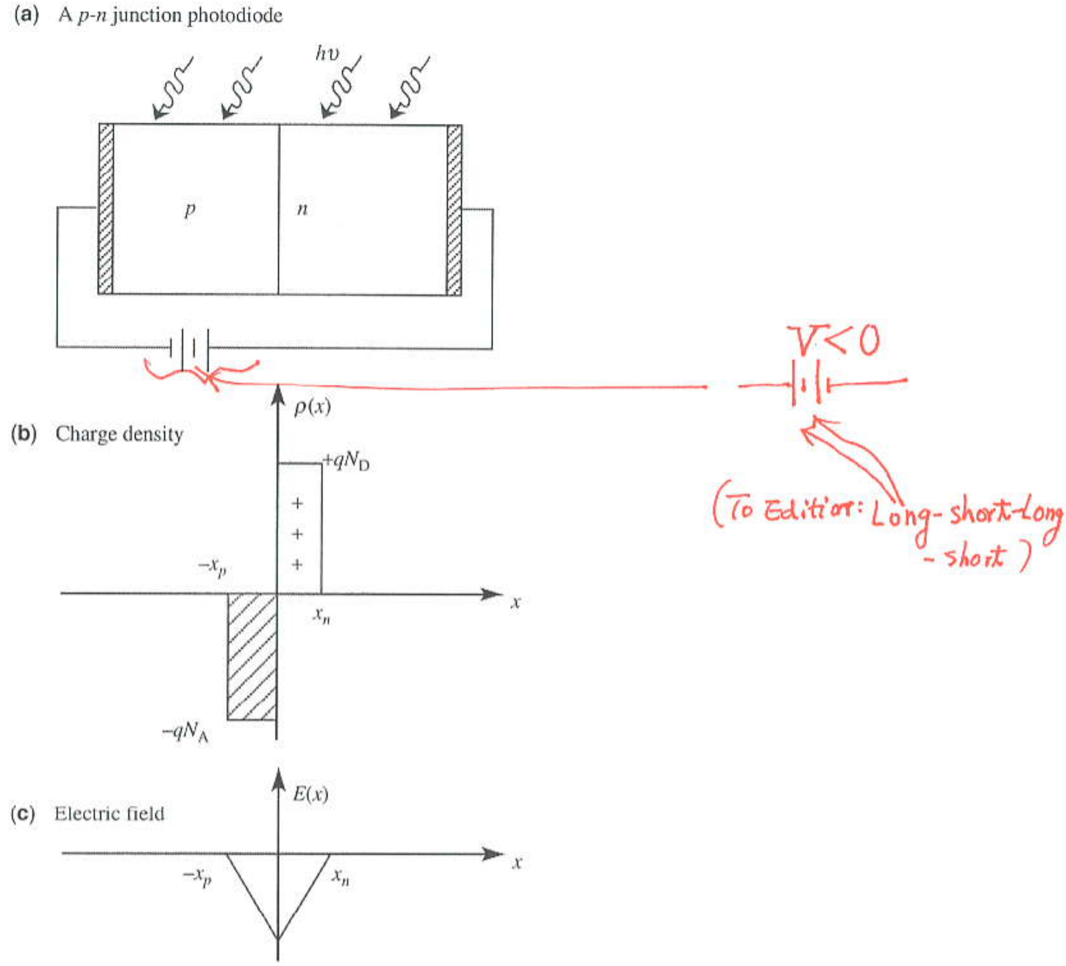

(To Editor: Long-short-Long - short)

Figure 15.4 (a) A *p-n* junction diode under the illumination of a uniform light. (b) The charge distribution $\rho(x)$ under depletion approximation. (c) The electric field $E(x)$ obtained from Gauss's law.

Because p_{n0} is independent of x and t, we have at steady state if $G(x, t) = G_0$ is independent of x and t,

$$D_p \frac{\partial^2}{\partial x^2} \delta p_n - \frac{\delta p_n}{\tau_p} = -G_0. \tag{15.2.3}$$

The above equation can be solved by summing the homogeneous and particular solutions

$$\delta p_n(x) = c_1 e^{-(x-x_n)/L_p} + c_2 e^{(x-x_n)/L_p} + G_0 \tau_p \tag{15.2.4}$$

where $L_p = \sqrt{D_p \tau_p}$ is the diffusion length for holes. The particular solution is due to the optical generation. If the *n*-region is very long, we can set $c_2 = 0$; otherwise,

(Note: long-short -)

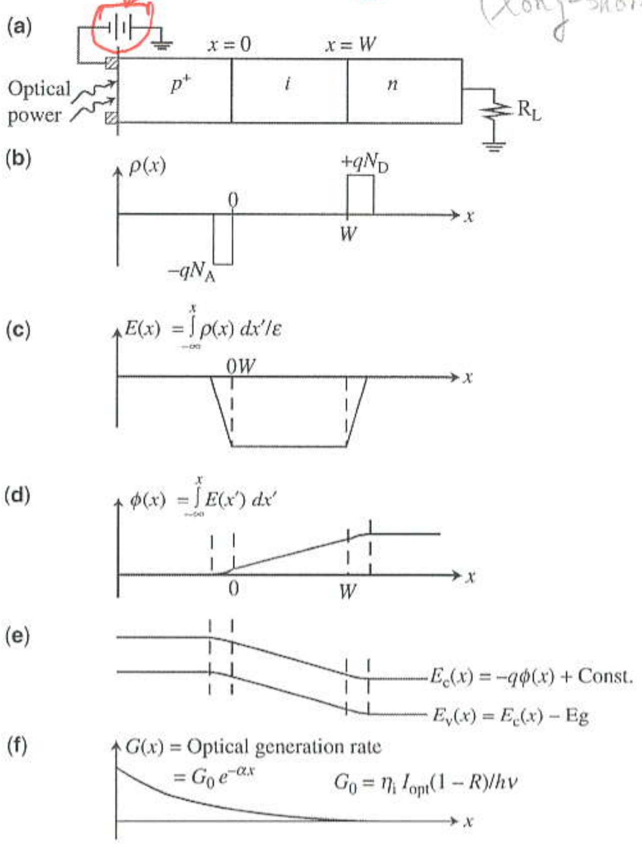

Figure 15.6 (a) A *p-i-n* photodiode under optical illumination from the p^+-side, (b) the charge density $\rho(x)$ under depletion approximation, (c) the static electric field profile $E(x)$, (d) the electrostatic potential $\varphi(x)$, (e) the conduction and valence band edge profiles, and (f) the optical generation rate $G(x)$.

ϕ

At steady state, the total photocurrent density consists of both a drift and a diffusion component

$$J = J_{\mathrm{dr}} + J_{\mathrm{diff}}. \tag{15.3.3}$$

Considering the p^+-region to be of negligible thickness, we look at the contribution in the intrinsic region $0 < x < W$

$$J_{\mathrm{dr}} = -q\int_0^W G(x)dx = -qS_0(1 - e^{-\alpha W}) = -q\eta\Phi(\lambda) \tag{15.3.4a}$$

$$\eta = \eta_i(1 - R)(1 - e^{-\alpha W}) \tag{15.3.4b}$$

where the minus sign of the drift current density accounts for the fact that the drift current flows in the $-x$ direction, and η is the quantum efficiency including the effects of surface reflectivity R and finite thickness of the absorption layer W.

proportional to the optical intensity profile in the device

$$G(x,\lambda) = G_0\,e^{-\alpha(\lambda)x}$$
$$G_0 = \eta_i[1 - R(\lambda)]\Phi(\lambda)\alpha(\lambda) \qquad (15.6.8)$$

$\alpha(\lambda)$

where $\cancel{\alpha}$ is the absorption spectrum, $\Phi(\lambda) = I_{\text{opt}}/\hbar\omega$ is the optical flux density for an incident optical power intensity I_{opt} (W/cm^2), and η_i is the intrinsic quantum efficiency to account for the average number (100% maximum) of electron–hole pairs generated per incident photon. Figure 15.21d shows the energy band diagram and the quasi-Fermi levels for a small forward bias voltage (defined as positive for the p-electrode). To obtain the I–V curve of a p-n junction solar cell, the key steps are essentially the same as those for photodiodes.

1. Find the minority carrier density in the quasi-neutral region of the n and p region in the presence of optical illumination with an incident photon flux (optical intensity) at a given wavelength λ for the given generation rate $G(x, \lambda)$. The major equations are the diffusion equations in the presence of carrier generation. The carrier densities or current densities have to satisfy the required boundary conditions.
2. Calculate the minority current density at the edge of the depletion region, that is, $J_p(\lambda)$ at $x = x_j$ ($= W_n - x_n$) on the n-side, and $J_n(\lambda)$ at $x = x_j + x_w$ the p-side, where x_w is the depletion width.
3. Calculate the contribution due to the drift current density due to optical generation in the depletion region $J_{\text{dr}}(\lambda)$

$$J_{\text{dr}}(\lambda) = q\int_{x_j}^{x_j+x_w} G_0 e^{-\alpha x}dx$$
$$= q\eta_i[1 - R(\lambda)]\Phi(\lambda)e^{-\alpha x_j}(1 - e^{-\alpha x_w}). \qquad (15.6.9)$$

4. The total current density for an incident photon flux at a given wavelength is

$$J(\lambda) = J_p(\lambda) + J_n(\lambda) + J_{\text{dr}}(\lambda). \qquad (15.6.10)$$

5. The spectral response is defined as

$$S_R(\lambda) = \frac{J(\lambda)}{q[1 - R(\lambda)]\Phi(\lambda)}. \qquad (15.6.11)$$

6. The total photocurrent is obtained by integrating the product of the transmitted photon flux into the solar cell and the spectral response to the maximum

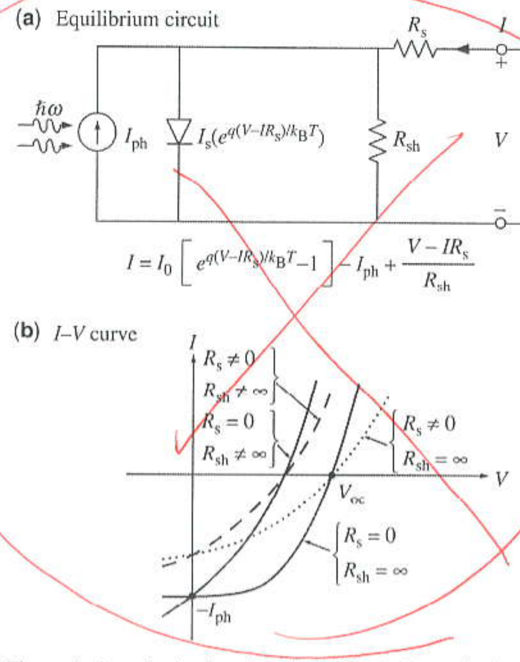

Use the Revised Fig. 15.23

Figure 15.23 (a) The equivalent circuit of a solar cell. (b) The I–V curve in the presence of shunt (R_{sh}) and series (R_s) resistances. In an ideal solar cell, the shunt resistance is infinity and the series resistance is zero.

conversion efficiency is reduced, as shown in Fig. 15.23b

$$I = I_0[e^{q(V-IR_s)/\gamma k_BT} - 1] - I_{ph} + \frac{V - IR_s}{R_{sh}}. \tag{15.6.25}$$

15.6.3 Quantum-Well and Multijunction Solar Cells

Quantum-Well Solar Cells By placing multiple quantum wells [111–121] in the intrinsic region of a *p-i-n* structure, it is possible to realize solar cells with improved quantum efficiency, Fig. 15.24. It is important to maintain the built-in field across

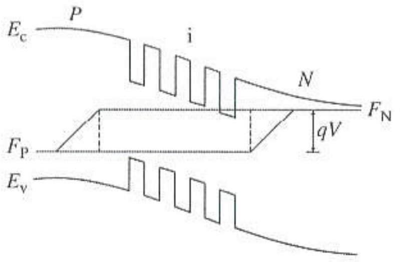

Figure 15.24 A multiple quantum-well (MQW) solar cell in a *P-I-N* structure. The intrinsic region contains many quantum wells for enhanced absorption.

(a) Energy band diagram

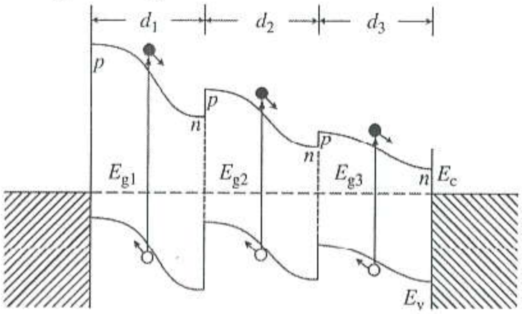

(b) Generation rate

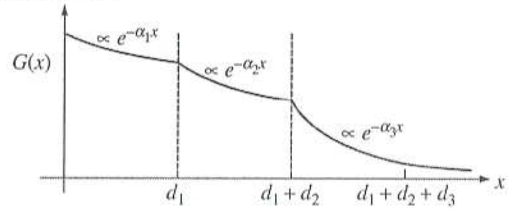

(c) Absorption spectrum

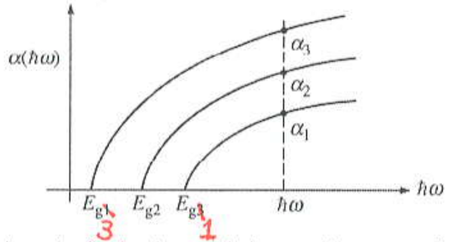

← Corrections (use Revised Fig. 15.26)

Figure 15.26 (a) The schematics for the electron–hole generation rate as a function of optical depth into the multijunction solar cell from the top wide band gap into the bottom narrow band gap region. (b) The generation rate of electron–hole pairs is proportional to the optical intensity, which decays as a function of position x. (c) The absorption spectra of the three band gaps.

can be lattice-matched to substrates such as Si, Ge, and GaAs, with band gaps that are complementary to those of other III–V compound semiconductors. The absorption spectra of some of these materials have been shown in Chapter 2, Fig. 2.4. Poor minority carrier transport in III-N-V materials is a critical research issue.

Figure 15.26a shows the schematic for the electron–hole generation rate as a function of optical depth into the multijunction solar cell from the top wide band gap into the bottom narrow band gap region. Figure 15.26b shows the generation rate per unit volume of the electron–hole pairs, which is proportional to the optical intensity that decays into the solar cell depth. The absorption spectra of all three band gaps are illustrated in Fig. 15.26c. The absorption of the solar radiation spectrum by different band gap layers allows for the conversion of more photons into electron and hole pairs. Carrier transport and collection become important

(a) Equilibrium Circuit

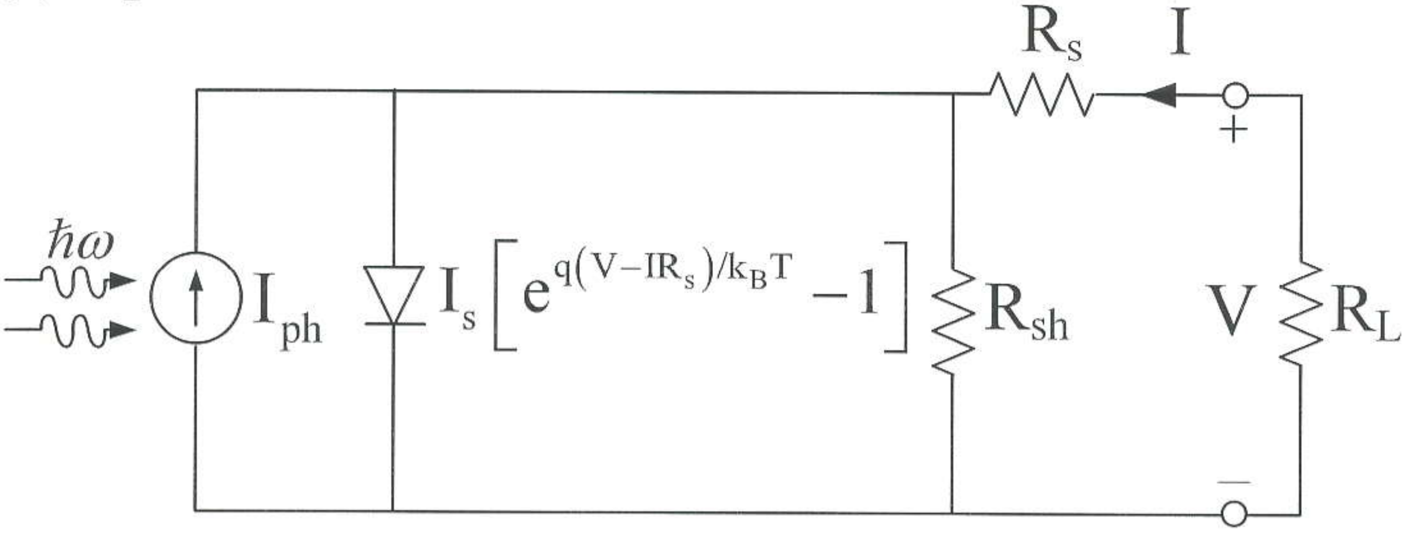

$$I=I_0\left[e^{q(V-IR_s)/k_BT}-1\right]-I_{ph}+\frac{V-IR_s}{R_{sh}}$$

(b) I-V Curve

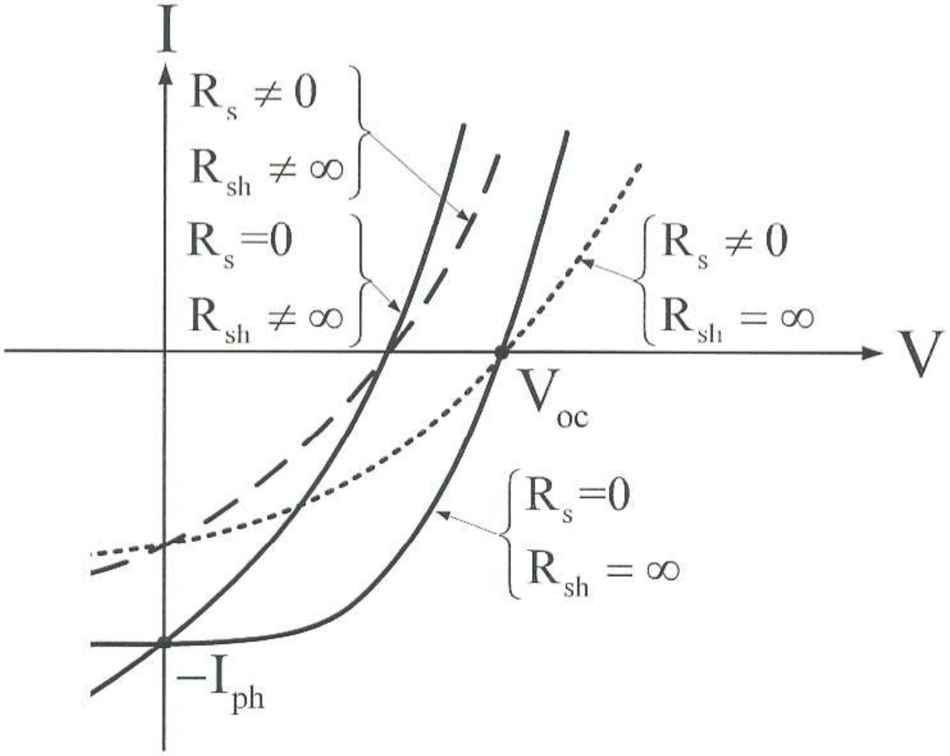

New (Revised) Figure 15.23

(a) Energy Band Diagram

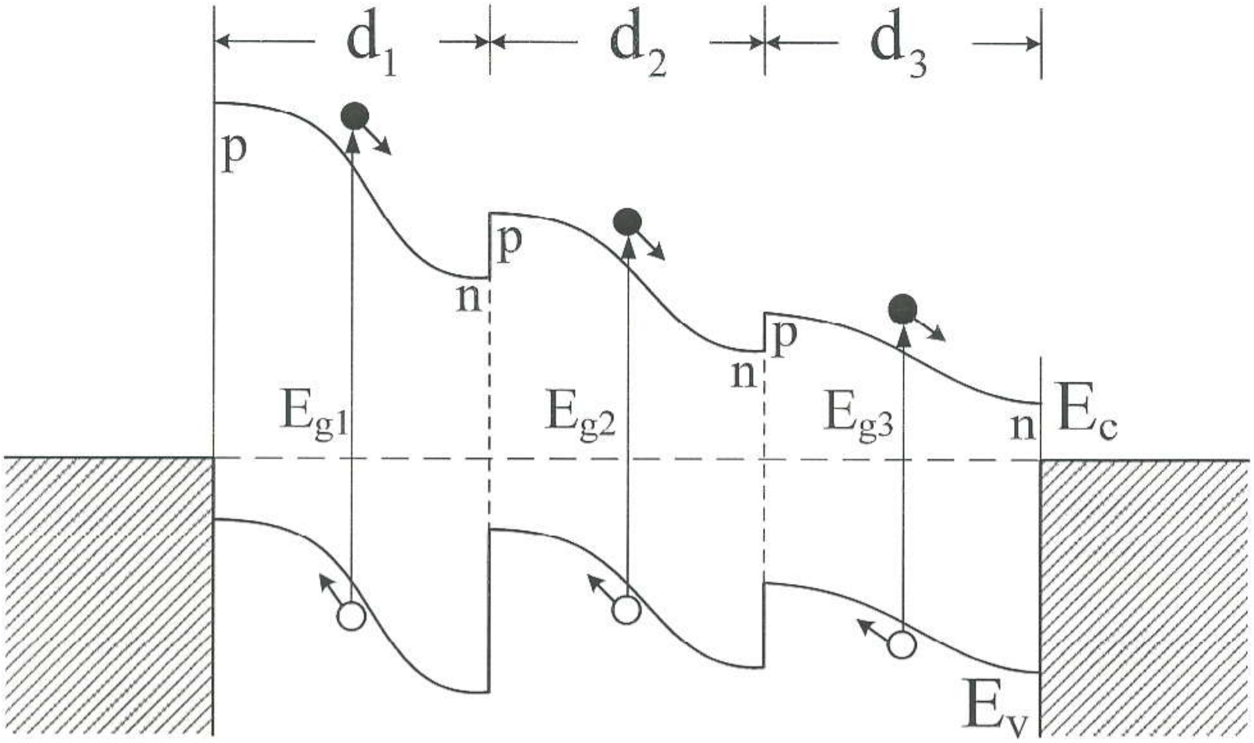

(b) Generation Rate

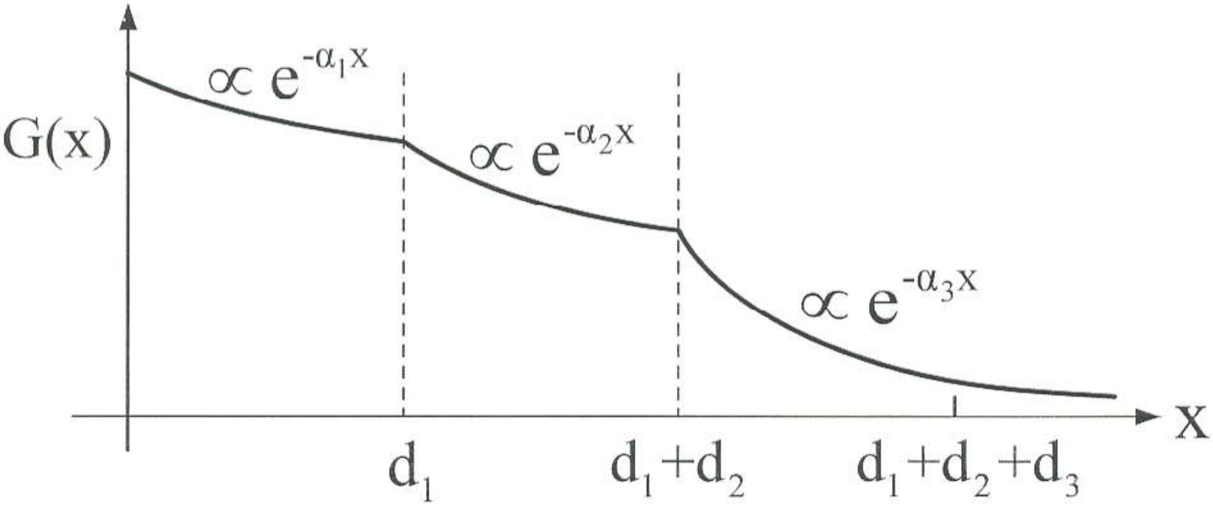

(c) Absorption Spectrum

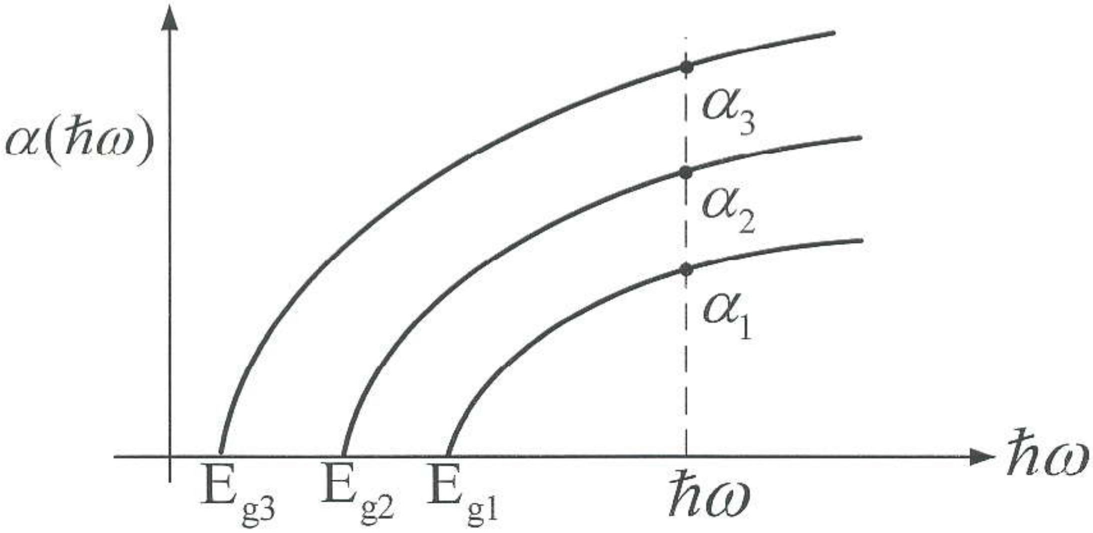

Revised
Fig.15.26

These two pages are missing in the First print.
This & the next page should be printed
in the inside of the Bottom Cover.

①

Physical Constants	Symbol	Numerical Values
Speed of light in free space	c	$= 2.9979 \times 10^{8}$ m/s
Permittivity in free space	ε_0	$= 8.8542 \times 10^{-12}$ F/m $\left(\simeq \frac{1}{36\pi} \times 10^{-9}\ \mathrm{F/m}\right)$
Permeability in free space	μ_0	$= 4\pi \times 10^{-7}$ H/m
Boltzmann constant	k_B	$= 1.3807 \times 10^{-23}$ J/K
Elementary charge	q or e	$= 1.60219 \times 10^{-19}$ C
Free electron mass	m_0	$= 9.1095 \times 10^{-31}$ kg
Planck constant	h	$= 6.6262 \times 10^{-34}$ Js
Reduced Planck constant	$\hbar = \frac{h}{2\pi}$	$= 1.05459 \times 10^{-34}$ Js $= 6.5822 \times 10^{-16}$ eVs
Angstrom unit	1 Å	$= 10^{-10}$ m $= 10^{-8}$ cm $= 10^{-4}$ μm
Bohr radius	$a_0 = \frac{4\pi\varepsilon_0\hbar^2}{e^2 m_0}$	$= 0.529177$ Å
Ryberg energy	$R_y = \frac{m_0 e^4}{2(4\pi\varepsilon_0)^2\hbar^2}$	$= \frac{\hbar^2}{2m_0}\left(\frac{1}{a_0}\right)^2 = 13.6058$ eV
Energy unit (electron-volt)	1 eV	$= 1.60219 \times 10^{-19}$ J
Thermal energy at 300 K	$k_B T$	$= 25.853$ meV

Useful Formulas and Physical Quantities	
Photon energy	$\hbar\omega = h\frac{c}{\lambda} = \frac{1.2398}{\lambda}$ eV, where λ is in (μm)
Rydberg of an exciton	$R_y = \frac{m_r e^4}{2(4\pi\varepsilon_s)^2\hbar^2} = \frac{(m_r/m_0)}{(\varepsilon_s/\varepsilon_0)^2} \times 13.6058$ eV
Bohr radius of an exciton	$a_0 = \frac{4\pi\varepsilon_s\hbar^2}{e^2 m_r} = \frac{\varepsilon_s/\varepsilon_0}{m_r/m_0} \times 0.529177$ Å
Quantized subband energy in a quantum well (infinite barrier model)	$E = \frac{\hbar^2}{2m^*}\left(\frac{n\pi}{L}\right)^2$ $= \frac{n^2}{(m^*/m_0)}\frac{1}{L^2} \times 37.6033$ eV (L is in Å)
Conduction band density parameter	$N_c = 2\left(\frac{m_e^* k_B T}{2\pi\hbar^2}\right)^{3/2} = 2.51 \times 10^{19}\left(\frac{m_e^*}{m_0}\frac{T}{300}\right)^{3/2}$ cm^{-3}

Inside the
Bottom Cover ②

---

(1) Maxwell's Equations

$$\nabla \times \mathbf{E} = -\frac{\partial}{\partial t}\mathbf{B}$$

$$\nabla \times \mathbf{H} = \mathbf{J} + \frac{\partial \mathbf{D}}{\partial t}$$

$$\nabla \cdot \mathbf{D} = \rho$$

$$\nabla \cdot \mathbf{B} = 0$$

Continuity Equation

$$\nabla \cdot \mathbf{J} + \frac{\partial}{\partial t}\rho = 0$$

(2) Semiconductor Electronics Equations

$$\nabla \cdot (\varepsilon \nabla \phi) = -q(p - n + N_D^+ - N_A^-)$$

$$\frac{\partial n}{\partial t} = G_n - R_n + \frac{1}{q}\nabla \cdot \mathbf{J}_n$$

$$\frac{\partial p}{\partial t} = G_p - R_p - \frac{1}{q}\nabla \cdot \mathbf{J}_p$$

$$\mathbf{J}_n = q\mu_n n\mathbf{E} + qD_n \nabla n$$

$$\mathbf{J}_p = q\mu_p p\mathbf{E} - qD_p \nabla p$$

$$\mathbf{E} = -\nabla \phi$$

(3) Density-of-States, $\rho_c\,(E)$

3D $\quad \dfrac{1}{2\pi^2}\left(\dfrac{2m_c^*}{\hbar^2}\right)^{3/2}\sqrt{E}$

2D $\quad \dfrac{m_c^*}{\pi \hbar^2 L_z}\displaystyle\sum_n H(E - E_n)$

1D $\quad \dfrac{1}{\pi L_x L_y}\sqrt{\dfrac{2m_c^*}{\hbar^2}}\displaystyle\sum_{n_x, n_y}\dfrac{1}{\sqrt{E - E_{n_x} - E_{n_y}}}$

(4) Fermi Distribution

Electron in conduction band

$$f_c(E) = \frac{1}{1 + e^{(E - F_c)/k_B T}}$$

Electron occupation probability in valence band

$$f_v(E) = \frac{1}{1 + e^{(E - F_v)/k_B T}}$$

Hole in valence band

$$f_h(E) = 1 - f_v(E) = \frac{1}{1 + e^{(F_v - E)/k_B T}}$$